Accepted Manuscript

Deformation patterning in finite-strain crystal plasticity by spectral homogenization with application to magnesium

A. Vidyasagar, Abbas D. Tutcuoglu, Dennis M. Kochmann

PII: S0045-7825(18)30120-8
DOI: https://doi.org/10.1016/j.cma.2018.03.003
Reference: CMA 11809

To appear in: *Comput. Methods Appl. Mech. Engrg.*

Received date : 5 December 2017
Revised date : 28 February 2018
Accepted date : 2 March 2018

Please cite this article as: A. Vidyasagar, A.D. Tutcuoglu, D.M. Kochmann, Deformation patterning in finite-strain crystal plasticity by spectral homogenization with application to magnesium, *Comput. Methods Appl. Mech. Engrg.* (2018), https://doi.org/10.1016/j.cma.2018.03.003

Deformation patterning in finite-strain crystal plasticity by spectral homogenization with application to magnesium

A. Vidyasagar[a,b], Abbas D. Tutcuoglu[a,b], Dennis M. Kochmann[a,b,*]

[a]*Mechanics & Materials, Department of Mechanical and Process Engineering, ETH Zürich, 8092 Zürich, Switzerland*
[b]*Graduate Aerospace Laboratories, California Institute of Technology, 91125 Pasadena, USA*

Abstract

Complex microstructural patterns arise as energy-minimizers in systems having non-convex energy landscapes such as those associated with phase transformations, deformation twinning, or finite-strain crystal plasticity. The prediction of such patterns at the microscale along with the resulting, effective material response at the macroscale is key to understanding a wide range of mechanical phenomena and has classically been dealt with by simplifying energy relaxation theory or by expensive finite element calculations. Here, we discuss a stabilized Fourier spectral technique for the homogenized response at the level of a representative volume element (RVE). We show that the FFT-based method admits sufficiently high resolution suitable to predict the emergence of energy-minimizing microstructures and the resulting effective response by computing the approximated quasiconvex energy hull. We test the method in the classical single-slip problem in single- and bicrystals. Especially the latter goes beyond the scope of traditional finite element and analytical relaxation treatments and hints at mechanisms of pattern formation in polycrystals. We also demonstrate that the chosen spectral finite-difference approximation, important for removing ringing artifacts in the presence of high contrasts, adds a natural regularization to the non-convex minimization. Finally, the technique is applied to polycrystalline pure magnesium, where we account for the competition between dislocation-mediated plasticity and deformation twinning. These inelastic deformation mechanisms result in complex texture evolution paths at the polycrystalline mesoscale and are simulated within RVEs of varying grain size and texture by a constitutive crystal plasticity model with an effective, volume fraction-based description of twinning.

Keywords: Homogenization, Spectral Methods, Polycrystal, Microstructure, Magnesium

1. Introduction

Magnesium (Mg) and magnesium alloys of various compositions have drawn interest for structural applications, primarily due to their high specific strength and low density (Pollock, 2010; Dixit et al., 2015). However, predicting the macroscopic mechanical response of bulk polycrystalline magnesium while also resolving the local fields, particularly interactions of twins with grain boundaries, presents an open challenge. The hexagonal closed-packed (hcp) crystal structure of Mg results in anisotropic inelastic deformation mechanisms (Graff et al., 2007; Stanford et al., 2011), remarkably low ductility and an asymmetric tension-compression behavior (Máthis et al., 2011; Park et al., 2014; Zachariah et al., 2013; Kurukuri et al., 2014). Dislocation slip and deformation twinning occur as competing mechanisms, and their mechanistic influences drive complex microstructure evolution paths observed in magnesium polycrystals (Agnew and Duygulu, 2005; Chang et al., 2017). It is hence important to understand and to enable the prediction of mesoscale microstructure evolution by high-fidelity methods to gain insight into the link between processing conditions, resulting microstructure and, ultimately, effective material properties. Simulations, in principle, must span a wide range of length and time scales to accurately capture interactions between twinning and dislocation slip, both of which are affected by the polycrystalline texture and grain size distribution. To this end, a combination of

*Phone +41-44-632-3276.
Email address: dmk@ethz.ch (Dennis M. Kochmann)

numerically efficient solvers and reliable constitutive models is required – an example of which will be demonstrated here.

Previous work in modeling Mg has involved atomistic investigations (Tomé et al., 2011; Wang et al., 2012), phase field models (Clayton and Knap, 2011), relaxation-based techniques (Homayonifar and Mosler, 2011, 2012), and various phenomenological continuum theories (Oppedal et al., 2013; Becker and Lloyd, 2016; Kalidindi, 2001; Izadbakhsh et al., 2011; Cheng and Ghosh, 2017; Zhang and Joshi, 2012). Each of these approaches have their advantages and drawbacks and aim for a compromise between accuracy and efficiency. One key differentiating aspect is the treatment of twins as either fully resolved in diffuse-interface and phase-field models (Clayton and Knap, 2011; Cheng and Ghosh, 2017), through pseudo-slip systems (Kalidindi, 2001; Zhang and Joshi, 2012) or as average twin variant volume fractions (Homayonifar and Mosler, 2011, 2012). Chang and Kochmann (2015) recently formulated a continuum constitutive model for Mg which combines conventional hcp crystal plasticity, accounting for the full set of hcp slip systems, with an effective description of the twin systems based on effective volume fractions; i.e., instead of resolving individual twin lamellae as in phase field approaches, the mesoscopic description only considers the effective volume fractions of twinned and untwinned phases at a given point on the continuum scale (thus being applicable at larger length scales). The reorientation of slip systems arising from deformation twinning is considered in a similar manner to previous work by Homayonifar and Mosler (2011, 2012) and Zhang and Joshi (2012). Chang et al. (2017) compared the performance of the model with reduced-order kinematic models and showed that lattice reorientation is critical for capturing experimentally observed behavior at large strains. However, the numerical inefficiencies of implementing the detailed constitutive model as compared to the reduced-order model within a conventional a finite element (FE) framework discourages its use in modeling the micro-to-macro transition. Therefore, we here report methods and results of periodic homogenization using spectral techniques along with a modified version of the constitutive model of Chang and Kochmann (2015) at the mesoscale of polycrystalline, pure Mg. Such periodic homogenization enables the prediction of microstructural evolution paths arising from various loading conditions and the extraction of the effective macroscopic stress-strain performance for comparisons to experimental observations. A key question in this context is the level of microstructural details required in order to reliably predict the effective macroscopic performance through a compromise of accuracy vs. efficiency.

Finite-deformation crystal plasticity models (especially those accounting for latent hardening and slip-twinning interactions) introduce numerical challenges. Particular loading paths result in a loss of quasiconvexity in regions of the energetic landscape. Energy relaxation in those regions is accomplished by breaking up the homogeneous deformation state into complex microstructural patterns (Ball, 1977; Ball and James, 1987) which result in energy-infimizing sequences; see, e.g., (Carstensen et al., 2002; Conti and Theil, 2005; Conti et al., 2009; Hackl and Kochmann, 2008; Kochmann and Hackl, 2011). Since those patterns are generally non-unique and the energy landscape offers numerous local minima, the prediction of minimizing microstructures (and the resulting stress-strain response as the volume average) is demanding. Previous work relied on either analytical energy relaxation (Miehe et al., 2004; Conti and Theil, 2005; Kochmann and Hackl, 2011) or on FE simulations (Carstensen and Plecháč, 1997; Bartels et al., 2006) to predict pattern formation. However, using low-order local FE interpolation with unregularized potentials results in coarse mesh- and interpolation-dependent microstructural patterns and heavy computational costs (Bartels et al., 2004; Bartels and Prohl, 2004). Regularization, e.g., by accounting for dislocation energies that depend on higher-order slip gradients, introduces a length scale, as was shown, e.g., by Klusemann and Kochmann (2014) who compared energy relaxation results to those of a continuum dislocation theory. However, like many prior studies, that analysis was limited to two dimensions (2D), assumed only a single active slip system and low hardening in a single-crystal for numerical feasibility.

Iterative Fourier spectral techniques have gained traction in recent years as tools for periodic homogenization. The matrix-free nature of the method and the quasi-linear scaling of its computational costs allow for polycrystal simulations at high resolution. Originally developed by (Moulinec and Suquet, 1998, 2003), who used a perturbation–correction strategy to account for nonlinear or inhomogeneous material behavior, it has since been extended and applied to a variety of material systems including large-deformation crystal visco-plasticity (Lahellec et al., 2003; Lebensohn et al., 2012; Eisenlohr et al., 2013; Lebensohn and Needleman, 2016) and multi-physics models (Brenner, 2009; Vidyasagar et al., 2017). Various methods have been developed to accelerate the convergence of the original Richardson scheme. Kabel et al. (2014) presented and compared several of these, including Newton-Raphson and Krylov subspace methods. Convergent, accelerated schemes stemming from the original formulation have been surveyed by Mishra et al. (2015). Spahn et al. (2014); Kochmann et al. (2016, 2017) extended this into a multi-

scale FE-FFT framework, while Shanthraj et al. (2015) compared computational costs of nonlinear Richardson and generalized minimal residual method (GMRES) spectral schemes.

The presence of high contrasts in mechanical properties (such as across composite interfaces or grain boundaries) presents a challenge for the original FFT method (Michel et al., 2001; Moulinec and Silva, 2014) in terms of both the convergence of the iterative solver (whose spectral radius relies on the initial guess for reference stiffness) and the appearance of numerical artifacts known as *ringing* and associated with the Gibbs phenomenon. First-order finite difference-based approximations composed onto Fourier transforms have been shown to result in significantly mitigating oscillatory artifacts (Müller, 1996; Brown et al., 2002; Berbenni et al., 2014; Brisard and Dormieux, 2010; Lebensohn and Needleman, 2016; Schneider et al., 2016), while maintaining consistency with the original governing equations with h-refinement. Willot et al. (2014) showed that rotated first-order schemes show a marked reduction in oscillatory artifacts. Similarly, the influence of higher-order finite-difference schemes on mitigating the ringing artifacts, ensuring convergence and smoothing out the fields, was surveyed by Vidyasagar et al. (2017) and showed promising results for nonconvex pattern prediction (in linearized kinematics applied to ferroelectric domain patterns).

Here, we beneficially combine several of the above approaches to study the microstructure formation and evolution in finite-strain crystal plasticity applied to polycrystalline Mg. The remainder of the paper is hence structured as follows. In Section 2, we briefly summarize the constitutive model for finite-strain plasticity in Mg. Next, in Section 3 we discuss the extension of the Fourier spectral setup of Vidyasagar et al. (2017) extended to finite strains for use in high-resolution crystal plasticity simulations. Due to the nonconvexity of the finite-deformation crystal plasticity model, patterns arise and we demonstrate the applicability of the scheme as a tool for quasiconvex pattern calculations for the classical example of single-slip plasticity in Section 4. In addition to single-crystals we also study bicrystals, which give rise to spatially inhomogeneous patterns due to the enforcement of compatibility across grain boundaries. Section 5 summarizes results of microstructure evolution and effective properties of polycrystalline Mg with varying grain size and texture, before concluding the present study in Section 6.

2. Constitutive model: finite-strain crystal plasticity in magnesium

We begin by briefly reviewing the constitutive model to the extent necessary for subsequent discussions; more details can be found in Chang and Kochmann (2015). The deformation at a point $\boldsymbol{x} \subset \Omega$ of a body Ω at time $t \geq 0$ is described by the deformation mapping $\varphi(\boldsymbol{X}, t) : \Omega \times t \to \mathbb{R}^n$. Under the assumption of isochoric plasticity, the deformation gradient $\boldsymbol{F}(\boldsymbol{X}, t) = \mathrm{Grad}(\varphi(\boldsymbol{X}, t))$ is multiplicatively decomposed into its elastic and inelastic parts, i.e., $\boldsymbol{F} = \boldsymbol{F}_\mathrm{e}\boldsymbol{F}_\mathrm{in}$. The hcp crystallography of Mg includes n_s slip systems, described by slip directions $\boldsymbol{s}_\alpha$ and normal vectors $\boldsymbol{m}_\alpha$. Similarly, the n_t twin systems are described by twin normals $\boldsymbol{n}_\beta$ and twinning shears $\boldsymbol{a}_\beta$. Dislocation slip is described by slips γ_α and twinning through effective twin volume fractions λ_β subject to the constraints

$$0 \leq \lambda_\beta \leq 1, \qquad 0 \leq \sum_{\beta=1}^{n_t} \lambda_\beta \leq 1. \tag{1}$$

The plastic velocity gradient tensor incorporates an additive decomposition into slip and twinning contributions, assuming these mechanisms occur simultaneously (with dots denoting material time derivatives):

$$\boldsymbol{l} = \dot{\boldsymbol{F}}\boldsymbol{F}^{-1} = \boldsymbol{l}_\mathrm{e} + \boldsymbol{l}_\mathrm{in} = \dot{\boldsymbol{F}}_\mathrm{e}\boldsymbol{F}_\mathrm{e}^{-1} + \boldsymbol{F}_\mathrm{e}\tilde{\boldsymbol{l}}_\mathrm{in}\boldsymbol{F}_\mathrm{e}^{-1}, \qquad \tilde{\boldsymbol{l}}_\mathrm{in} = \dot{\boldsymbol{F}}_\mathrm{in}\boldsymbol{F}_\mathrm{in}^{-1} = \tilde{\boldsymbol{l}}_\mathrm{p} + \tilde{\boldsymbol{l}}_\mathrm{tw}. \tag{2}$$

Following earlier works of Kalidindi (2001) and Zhang and Joshi (2012), the modified kinetic flow rule accounts for slip on untwinned and twinned phases. The crystallographic reorientation due to twinning is described by reflection tensors $\boldsymbol{Q}_\beta = \boldsymbol{I} - 2\boldsymbol{n}_\beta \otimes \boldsymbol{n}_\beta$ such that

$$\tilde{\boldsymbol{l}}_\mathrm{tw} = \sum_\beta \dot{\lambda}_\beta \boldsymbol{a}_\beta \otimes \boldsymbol{n}_\beta, \qquad \tilde{\boldsymbol{l}}_\mathrm{p} = \left[1 - \sum_\beta \lambda_\beta\right] \sum_\alpha \dot{\gamma}_\alpha \, \boldsymbol{s}_\alpha \otimes \boldsymbol{m}_\alpha + \sum_\beta \lambda_\beta \sum_\alpha \dot{\gamma}_\alpha \, \boldsymbol{Q}_\beta \boldsymbol{s}_\alpha \otimes \boldsymbol{Q}_\beta \boldsymbol{m}_\alpha. \tag{3}$$

The hardening behavior is captured by introducing the accumulated plastic slips ϵ_α, evolving according to $\dot{\epsilon}_\alpha = |\dot{\gamma}_\alpha|$. The thermodynamic description is based on the Helmholtz free energy density

$$A(\boldsymbol{F}_\mathrm{e}, \boldsymbol{\epsilon}, \boldsymbol{\lambda}) = W_\mathrm{e}(\boldsymbol{F}_\mathrm{e}) + W_\mathrm{p}(\boldsymbol{\epsilon}) + W_\mathrm{tw}(\boldsymbol{\lambda}), \tag{4}$$

containing, respectively, elastic, slip and twin contributions and depending on the internal variables $\boldsymbol{\lambda} = \{\lambda_1, \ldots, \lambda_{n_t}\}$, $\boldsymbol{\gamma} = \{\gamma_1, \ldots, \gamma_{n_s}\}$ and $\boldsymbol{\epsilon} = \{\epsilon_1, \ldots, \epsilon_{n_s}\}$. For simplicity, the elastic energy density is assumed approximately isotropic and taken as that of a compressible Neo-Hookean solid (μ and κ are, respectively, the shear and bulk moduli)[1]:

$$W_{\mathrm{e}}(\boldsymbol{F}_{\mathrm{e}}) = \frac{\mu}{2}\left(\operatorname{tr}\overline{\boldsymbol{C}}_e - 3\right) + \frac{\kappa}{2}(J-1)^2, \qquad \overline{\boldsymbol{C}}_{\mathrm{e}} = \overline{\boldsymbol{F}}_{\mathrm{e}}^{\mathrm{T}}\overline{\boldsymbol{F}}_{\mathrm{e}}, \quad \overline{\boldsymbol{F}}_{\mathrm{e}} = \frac{\boldsymbol{F}_{\mathrm{e}}}{J^{1/3}}, \quad J = \det \boldsymbol{F}. \tag{5}$$

The stored plastic energy density accounts for latent and self-hardening for each slip system, formulated as

$$W_{\mathrm{p}}(\boldsymbol{\epsilon}) = \frac{1}{2}\boldsymbol{\epsilon}\cdot\mathcal{H}\boldsymbol{\epsilon} + \begin{cases} \frac{h_0}{2}\epsilon_\alpha^2 & \text{for basal systems,} \\ \sigma_\infty\left[\epsilon_\alpha + \frac{\sigma_\infty}{h}\exp\left(-\frac{h_0\,\epsilon_\alpha}{\sigma_\infty}\right)\right] & \text{for prismatic and pyramidal systems,} \end{cases} \tag{6}$$

where $\mathcal{H}$ indicates the latent slip hardening matrix. The parameters are specific to each slip system and given in Appendix B. Similarly, the stored twin energy is assumed of the form

$$W_{\mathrm{tw}}(\boldsymbol{\lambda}) = \frac{1}{2}\boldsymbol{\lambda}\cdot\mathcal{K}\boldsymbol{\lambda} + \frac{h_\beta}{2}\lambda_\beta^2, \tag{7}$$

where $\mathcal{K}$ indicates the twin interaction matrix. As discussed in Chang and Kochmann (2015), simultaneous multiple twin systems at a single point are avoided by high latent twin hardening (i.e., high values of the off-diagonal components of the twin hardening matrix $\mathcal{K}$).

The rate-dependent evolution laws for slip and twinning are defined by dual dissipation potentials $\Psi_{\mathrm{p}}^*(\dot{\boldsymbol{\gamma}})$ and $\Psi_{\mathrm{tw}}^*(\dot{\boldsymbol{\lambda}})$, respectively, akin to previous approaches in crystal plasticity; see, e.g., Ortiz and Stainier (1999):

$$\Psi_{\mathrm{p}}^*(\dot{\boldsymbol{\gamma}}) = \sum_\alpha \frac{\tau_0\dot{\gamma}_0}{m+1}\left(\frac{\dot{\gamma}_\alpha}{\dot{\gamma}_0}\right)^{m+1}, \qquad \Psi_{\mathrm{tw}}^*(\dot{\boldsymbol{\lambda}}) = \sum_\beta \frac{\eta_\beta}{2}\dot{\lambda}_\beta^2 \tag{8}$$

with reference slip rate $\dot{\gamma}_0$, hardening exponent m, back-stress τ_0, and twin resistance (inverse mobility) η for each system. Note that in contrast to the rate-independent formulation of Chang and Kochmann (2015), we here adopt the rate-dependent formulation for twinning from (Chang et al., 2017) with the above quadratic dissipation potential to facilitate a simple explicit update scheme for slip and twinning (to be discussed in Section 3.2).

The principle of minimum dissipation potential (Ortiz and Repetto, 1999; Carstensen et al., 2002; Conti and Ortiz, 2008; Hackl and Fischer, 2008) is invoked to derive the evolution laws for the internal variables $\boldsymbol{\gamma}$ and $\boldsymbol{\lambda}$, viz.

$$0 \in \frac{\partial}{\partial\dot{\boldsymbol{\gamma}}}\left(\dot{A} + \Psi_{\mathrm{p}}^*\right), \qquad 0 \in \frac{\partial}{\partial\dot{\boldsymbol{\lambda}}}\left(\dot{A} + \Psi_{\mathrm{tw}}^*\right). \tag{9}$$

For the rate-dependent model considered here, the differential inclusions can be replaced by equalities. Minimizing the total stress power using (9) results in the kinetic update rules

$$\begin{aligned} \dot{\gamma}_\alpha &= \left(\frac{|\tau_\alpha^{\mathrm{p}}| - \tau_\alpha^h}{\tau_0}\right)^{\frac{1}{m}} \quad \text{with} \quad \tau_\alpha^h = \sum_\zeta h_{\alpha\zeta}\epsilon_\zeta + \begin{cases} h_0\epsilon_\alpha & \text{for basal systems,} \\ \sigma_\infty\left[1 - \exp\left(-\frac{h_0\,\epsilon_\alpha}{\sigma_\infty}\right)\right], & \text{for prismatic and pyramidal systems,} \end{cases} \\ \dot{\lambda}_\beta &= \frac{\tau_\beta^{\mathrm{tw}} - \tau_\beta^h}{\eta_\beta} \quad \text{with} \quad \tau_\beta^h = \sum_\zeta k_{\beta\zeta}\lambda_\zeta + h_0\lambda_\beta, \end{aligned} \tag{10}$$

where τ_α and τ_β are the resolved shear stresses on the respective slip and twin systems.

[1] The elastic anisotropy is relatively mild and was shown to have little effect on the effective material response (Chang and Kochmann, 2015).

3. Spectral homogenization scheme

3.1. Fourier spectral method and finite-difference approximation

The above material model is used to solve quasistatic mechanical boundary value problems governed by the conservation of linear momentum balance, i.e.,

$$\operatorname{Div} \boldsymbol{P} = \boldsymbol{0} \qquad \text{in a body } \Omega, \tag{11}$$

where $\boldsymbol{P}$ denotes the first Piola-Kirchhoff stress tensor in the undeformed (material) configuration. Periodic boundary conditions are applied to a representative volume element (RVE) such that for an average deformation gradient $\boldsymbol{F}^0$

$$\boldsymbol{x}^+ - \boldsymbol{x}^- = \boldsymbol{F}^0(\boldsymbol{X}^+ - \boldsymbol{X}^-), \qquad \boldsymbol{F}^0 = \frac{1}{|\Omega|}\int_\Omega \boldsymbol{F}(\boldsymbol{X})\,\mathrm{d}V, \tag{12}$$

where $\boldsymbol{x}^\pm$ and $\boldsymbol{X}^\pm$ are, respectively, deformed and undeformed positions on opposite surfaces of the RVE. Following Moulinec and Suquet (1998, 2003); Lebensohn et al. (2012), we introduce the perturbation stress tensor $\boldsymbol{\tau}(\boldsymbol{x})$ such that

$$\boldsymbol{P}(\boldsymbol{X}) = \mathbb{C}^0\,\boldsymbol{F}(\boldsymbol{X}) - \boldsymbol{\tau}(\boldsymbol{X}) \qquad \text{in } \Omega \tag{13}$$

with a reference modulus tensor $\mathbb{C}^0$ that can be taken, e.g., as the average

$$\mathbb{C}^0_{iJkL} = \frac{1}{V}\int_V \mathbb{C}_{iJkL}(\boldsymbol{X})\,\mathrm{d}V, \qquad \mathbb{C}_{iJkL}(\boldsymbol{X}) = \frac{\partial^2 A}{\partial F_{iJ}\,\partial F_{kL}}, \tag{14}$$

which we evaluate in the current, deformed configuration. The resulting average modulus tensor is positive-definite as long as the RVE is stable. While the choice of $\mathbb{C}^0$ affects the convergence behavior of the chosen iterative scheme, it does not affect the equilibrium solution. By using the kinematic relation $\boldsymbol{F}(\boldsymbol{X}) = \operatorname{Grad}\boldsymbol{\varphi}(\boldsymbol{X})$, insertion of (13) into (11) gives (using indicial notation with summation convention)

$$\left[\mathbb{C}^0_{iJkL}\,\varphi_{k,L}(\boldsymbol{X}) - \tau_{iJ}(\boldsymbol{X})\right]_{,J} + RB_i(\boldsymbol{X}) = 0 \qquad \text{in } \Omega. \tag{15}$$

We discretize the RVE into a regular grid. Application of a discrete (inverse) Fourier transform to the quasistatic deformation mapping $\boldsymbol{\varphi}(\boldsymbol{X})$ yields

$$\boldsymbol{\varphi}(\boldsymbol{X}) = \sum_{\boldsymbol{K}\in\mathcal{T}} \hat{\boldsymbol{\varphi}}(\boldsymbol{K})\,\exp\left(-ih\boldsymbol{K}\cdot\boldsymbol{X}\right), \qquad h = \frac{2\pi}{n} \quad \text{and} \quad i = \sqrt{-1} \tag{16}$$

with the reciprocal lattice $\mathcal{T} = \{\boldsymbol{K}_1, \ldots, \boldsymbol{K}_n\}$ in $\boldsymbol{K}$-space chosen to ensure periodicity. Analogous transformations are applied to $\boldsymbol{\tau}(\boldsymbol{X})$. When assuming negligible body forces, this turns (15) into

$$\mathbb{A}_{ik}\,\hat{\varphi}_k(\boldsymbol{K}) = \frac{i}{h}\hat{\tau}_{iJ}(\boldsymbol{K})\,K_J \qquad \text{with the acoustic tensor} \quad \mathbb{A}_{ik}(\boldsymbol{K}) = \mathbb{C}^0_{iJkL}\,K_J\,K_L. \tag{17}$$

Note that $\mathbb{A}(\boldsymbol{K})$ is invertible only if $\boldsymbol{K} \neq \boldsymbol{0}$. For the special case $\boldsymbol{K} = \boldsymbol{0}$ we must have $\hat{\boldsymbol{F}}(\boldsymbol{0}) = \boldsymbol{F}^0$. Using $\hat{F}_{iJ} = -ih\hat{\varphi}_i K_J$, we solve for the deformation gradient, resulting in

$$\hat{F}_{kL}(\boldsymbol{K}) = \begin{cases} \mathbb{A}^{-1}_{ik}(\boldsymbol{K})\hat{\tau}_{iJ}(\boldsymbol{K})K_J K_L & \text{for } \boldsymbol{K} \neq \boldsymbol{0} \\ F^0_{kL} & \text{for } \boldsymbol{K} = \boldsymbol{0}. \end{cases} \tag{18}$$

Note that $\boldsymbol{\tau}$ depends on $\boldsymbol{F}$, so that an iterative solver is required in general (see Section 3.2).

The standard spectral scheme described above, in the presence of discontinuities in $\boldsymbol{\tau}(\boldsymbol{X})$ and $\boldsymbol{F}(\boldsymbol{X})$, exhibits numerical ringing artifacts associated with the Gibbs phenomenon for truncated Fourier series (Gibbs, 1898, 1899; Hewitt and Hewitt, 1979). Inspired by Willot et al. (2014), Berbenni et al. (2014) and Lebensohn and Needleman (2016), we use discrete (modified) spectral differentiation with a finite difference-based scheme (Müller, 1996). The simplest of these modified schemes for a uniform grid with spacing ΔX, whose derivation was presented in detail in

Vidyasagar et al. (2017), is a discrete analog of the Lanczos-$\boldsymbol{\sigma}$ factor (Lanczos, 1956). By applying a central-difference approximation to spatial derivatives before Fourier transform, one arrives at the approximation

$$\mathcal{F}\left(\frac{\partial f}{\partial X_i}\right) = -ihK_i\mathcal{F}(f) \approx -\frac{i\sin(hK_i\Delta X)}{\Delta X}\mathcal{F}(f), \tag{19}$$

which converges to the exact derivative with decreasing grid size ($\Delta X \to 0$). The above can be extended to rotated (Willot et al., 2014) and higher-order schemes (Vidyasagar et al., 2017) by choosing different finite-difference stencils.

To avoid ringing artifacts in the following, we use a 12th-order central-difference stencil (derived in Appendix C), which leads to the approximation

$$\begin{aligned}\mathcal{F}\left(\frac{\partial f}{\partial X_i}\right) \approx -\frac{i}{13860\,\Delta X}\Big[&23760\,\sin(h\,K_i\,\Delta X) - 7425\,\sin(2\,h\,K_i\,\Delta X) + 2200\,\sin(3\,h\,K_i\,\Delta X)\\ &- 495\,\sin(4\,h\,K_i\,\Delta X) + 72\,\sin(5\,h\,K_i\,\Delta X) - 5\,\sin(6\,h\,K_i\,\Delta X)\Big]\mathcal{F}(f(\boldsymbol{X})).\end{aligned} \tag{20}$$

3.2. *Numerical solution strategy – explicit updates*

The above equations are solved in an incremental, staggered fashion for the unknown fields $\boldsymbol{F}(\boldsymbol{X})$, $\boldsymbol{\lambda}(\boldsymbol{X})$ and $\boldsymbol{\gamma}(\boldsymbol{X})$ at the RVE grid points, using an explicit scheme. First, at each load step $n+1$, with a known $(\boldsymbol{F}^0)^{n+1}$ the elastic problem is solved assuming constant internal variables,

$$F_{kL}^{n+1}(\boldsymbol{X}) = \mathcal{F}^{-1}\{\hat{F}_{kL}^{n+1}(\boldsymbol{K})\} \qquad \text{and} \qquad \hat{F}_{kL}^{n+1}(\boldsymbol{K}) = \begin{cases}\mathbb{A}_{ik}^{-1}(\boldsymbol{K})\hat{\tau}_{iJ}^{n+1}(\boldsymbol{K})K_JK_L & \text{for } \boldsymbol{K}\neq\boldsymbol{0}\\ (F_{kL}^0)^{n+1} & \text{for } \boldsymbol{K}=\boldsymbol{0}.\end{cases} \tag{21}$$

The nonlinear equations are solved using a fixed-point iteration scheme. Due to the nonlinearity of the elastic problem, the deformation-dependent acoustic tensor $\mathbb{A}$ is re-evaluated periodically during the iterations. Next, the internal variables are updated in real space at each material point, with the update for slip activity given by

$$\gamma_\alpha^{n+1} = \gamma_\alpha^n + \Delta\gamma_\alpha^n = \gamma_\alpha^n + \dot{\gamma}_\alpha^0\Delta t\left(\frac{|\tau_\alpha^{\mathrm{p}}| - \tau_\alpha^{\mathrm{cr}}}{\tau_\alpha^0}\right)^{\frac{1}{m}} \tag{22}$$

with

$$\tau_\alpha^{\mathrm{p}} = \left(\boldsymbol{F}_{\mathrm{e}}^{\mathrm{T}}\frac{\partial \mathrm{W}_{\mathrm{e}}}{\partial \boldsymbol{F}}\boldsymbol{F}_{\mathrm{in}}^{\mathrm{T}}\right)\cdot\left(\left(1-\sum_\beta\lambda_\beta^n\right)\boldsymbol{s}_\alpha\otimes\boldsymbol{m}_\alpha + \sum_\beta\lambda_\beta^n\boldsymbol{Q}_\beta\boldsymbol{s}_\alpha\otimes\boldsymbol{Q}_\beta\boldsymbol{m}_\alpha\right) \quad \text{and} \quad \tau_\alpha^{\mathrm{cr}} = \frac{\partial W_{\mathrm{p}}(\boldsymbol{\gamma})}{\partial\gamma_\alpha}, \tag{23}$$

both to be evaluated at the previous load step n. The update for the twin volume fractions follows analogously as

$$\lambda_\beta^{n+1} = \lambda_\beta^n + \Delta\lambda_\beta^n = \lambda_\beta^n + \dot{\lambda}_\beta^0\Delta t\left(\frac{\tau_\beta^{\mathrm{tw}} - \tau_\beta^{\mathrm{cr}}}{\tau_\beta^0}\right) \tag{24}$$

with

$$\tau_\beta^{\mathrm{tw}} = \bar{\gamma}_\beta^{\mathrm{tw}}\left(\boldsymbol{F}_{\mathrm{e}}^{\mathrm{T}}\frac{\partial \mathrm{W}_{\mathrm{e}}}{\partial \boldsymbol{F}}\boldsymbol{F}_{\mathrm{in}}^{\mathrm{T}}\right)\cdot\left(\boldsymbol{a}_\beta\otimes\boldsymbol{n}_\beta\right) \quad \text{and} \quad \tau_\beta^{\mathrm{cr}} = \frac{\partial W_{\mathrm{tw}}(\boldsymbol{\lambda})}{\partial\lambda_\beta}, \tag{25}$$

again to be evaluated at step n. Finally, the inelastic deformation gradient is evaluated by a linearized forward-Euler step, using the slip and twin updates. In order to suppress numerical errors and to ensure that the inelastic deformation gradient is volume-preserving, we take only the deviatoric part of the update, resulting in

$$\begin{aligned}\boldsymbol{F}_{\mathrm{in}}^{n+1} &= \mathrm{dev}\left(\boldsymbol{F}_{\mathrm{in}}^n + \Delta t\,\tilde{\boldsymbol{l}}_{\mathrm{in}}\boldsymbol{F}_{\mathrm{in}}^n\right)\\ &= \mathrm{dev}\left[\boldsymbol{I} + \sum_{\alpha=1}^{n_s}\Delta\gamma_\alpha^n\left(1-\sum_\beta\lambda_\beta^n\right)\boldsymbol{s}_\alpha\otimes\boldsymbol{m}_\alpha + \sum_\beta\lambda_\beta^n\boldsymbol{Q}_\beta\boldsymbol{s}_\alpha\otimes\boldsymbol{Q}_\beta\boldsymbol{m}_\alpha + \sum_{\beta=1}^{n_t}\Delta\lambda_\beta^n\bar{\gamma}_\beta^{\mathrm{tw}}\left(\boldsymbol{a}_\beta\otimes\boldsymbol{n}_\beta\right)\right]\boldsymbol{F}_{\mathrm{in}}^n.\end{aligned} \tag{26}$$

3.3. Finite difference-induced regularization

Important to our subsequent analyses, finite-difference spectral differentiation of the type (19) introduces an artificial contribution to the energy; in other words, the smearing out of sharp contrasts in the primary fields (here, the deformation mapping and its gradients) into diffuse interfaces results in an artificial interface energy, which introduces a relative, numerical length scale that can be visible in simulated results. The term *interface* energy here refers to a gradient contribution in the energy functional to be minimized (not a material interface). Every finite-difference approximation introduces an error of order $O(\Delta X^n)$. For example, the second-order central-difference stencil leading to the approximation (19) is second-order accurate, i.e., $O(\Delta X^2)$. Therefore, we may write the approximate deformation gradient $\boldsymbol{F}^h$ (with components $F^h_{mN} = \varphi^h_{m,N}$) resulting from the approximate solution $\boldsymbol{\varphi}^h$ at any point $\boldsymbol{X}_0 \in \Omega$ as

$$\varphi^h_{m,N}(\boldsymbol{X}_0) = \varphi_{m,N}(\boldsymbol{X}_0) + \frac{(\Delta X)^2}{6}\frac{\partial^3 \varphi_m}{\partial X_N^3}(\boldsymbol{X}_0) + O(\Delta X^4). \tag{27}$$

In case of the Neo-Hookean energy density in (5), performing a matrix Taylor expansion with $\boldsymbol{F}_\mathrm{e} = \boldsymbol{F}\boldsymbol{F}_\mathrm{in}^{-1}$ yields the additional energy contribution W^h to the elastic strain energy density W_e due to the finite difference-based modified Fourier transform (see Appendix D). Specifically, the total elastic energy density is now obtained as

$$\widetilde{W}_\mathrm{e} = W_\mathrm{e} + W^h + O(\Delta X^{n+2}), \qquad W^h = \frac{(\Delta X)^n}{2(n+1)!}\left(2\kappa(J-1)J\,\mathrm{tr}\left(\boldsymbol{F}_\mathrm{e}^{-1}\boldsymbol{G}^{(n)}\right) - \frac{\mu}{J^{2/3}}\left[\mathrm{tr}\,\boldsymbol{C}_\mathrm{e}\,\mathrm{tr}\left(\boldsymbol{F}_\mathrm{e}^{-1}\boldsymbol{G}^{(n)}\right) - 3\,\mathrm{tr}\left((\boldsymbol{G}^{(n)})^\mathrm{T}\boldsymbol{F}_\mathrm{e}\right)\right]\right) \tag{28}$$

where

$$G^{(n)}_{iJ} = \sum_\nu \frac{\partial^{n+1}\varphi_i}{\partial X_\nu^{n+1}}(\boldsymbol{X}_0)\left(\boldsymbol{F}_\mathrm{in}^{-1}(\boldsymbol{X}_0)\right)_{\nu J} = \sum_\nu \frac{\partial^n F_{i\nu}}{\partial X_\nu^n}(\boldsymbol{X}_0)\left(\boldsymbol{F}_\mathrm{in}^{-1}(\boldsymbol{X}_0)\right)_{\nu J}. \tag{29}$$

The approximate energy density thus includes a gradient regularization term, dependent to leading order on the third-order deformation gradient tensor $\boldsymbol{G} = \mathrm{Grad}\,\boldsymbol{F}$. The aforementioned regularization ensures that the solution is smooth to the order of the higher-gradient energy contribution. Where the unregularized problem (without finite-difference correction) would lead to sharp interfaces and strong jumps in the local properties (e.g., deformation gradient or plastic slips) and consequently noticeable ringing artifacts, the regularized problem (with finite-difference approximation) smears out sharp contrast over a small but finite interface. While consistency is ensured in the limit of vanishing grid spacing $\Delta X \to 0$, the presence of a penalization on higher-order gradients introduces non-locality and regularizes the deformation gradient field $\boldsymbol{F}(\boldsymbol{X})$, which becomes apparent when modeling, e.g., the formation of laminate patterns: pure energy relaxation assumes sharp interfaces without interfacial energy and therefore yields effective volume fractions but no intrinsic length scale, whereas the above approximation does provide such a relative length scale (dependent on grid resolution). This in turn ensures that the spectral approximation is beneficially convergent when using an explicit scheme. Note that for a given number of grid points, ΔX scales with the size of the RVE, so that the introduced length scale is *relative* with respect to the size of the RVE. Thus, it does not provide a physical length scale as, e.g., in gradient or nonlocal plasticity models (Klusemann and Kochmann, 2014). This in turn implies that the width of the diffuse interfaces should not be interpreted as exact, which comes with the numerical benefit that grid resolution does not need to recover the oftentimes atomically-sharp interfaces; see, e.g., Vidyasagar et al. (2017).

The above setup can be extended to higher-order correction schemes such as the twelfth-order central-difference stencil leading to (20). The latter is used in Section 4 in comparison to the second-order spectral scheme (19) in order to perform benchmark tests for the numerical computation of relaxed energies and microstructures in crystal plasticity. We find that the twelfth-order stencil is sufficiently high to limit the interface thickness in all simulations. This is a compromise between using a higher-order scheme such that the interfaces are thin (ideally to recover the sharp interface limit) while having suffcient grid resolution to capture the interfaces accurately. Vidyasagar et al. (2017) showed the convergence and accuracy of various finite-difference stencils in linear elasticity (from second to eighth order). The influence of such regularization on the topological nature of pattern interfaces will be demonstrated and discussed in Section 4.

4. Microstructural patterns in single-slip crystal plasticity

4.1. Loss of quasiconvexity in single-crystals

Non-convex potentials describe multistable physical systems and arise, e.g., from phase transitions and phase transformations, during deformation twinning and in finite-strain crystal plasticity. When loaded, such systems produce complex microstructural patterns as energy-infimizing sequences (Ball, 1977; Ball and James, 1987); see also Carstensen et al. (2002); Conti and Theil (2005); Kochmann and Hackl (2011) for examples in single-slip crystal plasticity. Instead of following the energetically unfavorable nonconvex energy landscape, such materials form patterns at the microstructural level (i.e., inhomogeneous states of deformation) to reduce their energy below that of a homogeneous state of deformation, thereby following the quasiconvex envelope of the energy. Numerical calculation of the quasiconvex envelope or approximations thereof (most commonly the rank-one-convex hull) is challenging because of many local minima, mesh dependence (of finite element schemes) and computational costs. As summarized below, the finite-strain crystal plasticity model employed here also displays nonconvexity along certain loading paths, which is why we proceed to study the numerical stability of and the patterns predicted by our spectral scheme.

We consider first the special case of only a single active slip system with no active twin systems, so the internal variables reduce to γ and ϵ. Consequently, the inelastic deformation gradient and velocity gradient can be integrated to give

$$\tilde{\boldsymbol{l}}_{\text{in}} = \tilde{\boldsymbol{l}}_{\text{p}} = \dot{\gamma}\, \boldsymbol{s} \otimes \boldsymbol{m} \qquad \Rightarrow \qquad \boldsymbol{F}_{\text{in}} = \boldsymbol{I} + \gamma\, \boldsymbol{s} \otimes \boldsymbol{m}. \tag{30}$$

This results in the energy density

$$A(\boldsymbol{F}, \epsilon) = \frac{\mu}{2}\left(\widetilde{I}_{\text{e},1} - 3\right) + \frac{\kappa}{2}(J-1)^2 + \sigma^{\infty}\left[\epsilon + \frac{\sigma^{\infty}}{h}\exp\left(-\frac{h\,\epsilon}{\sigma^{\infty}}\right)\right] + \frac{H}{2}\epsilon^2, \tag{31}$$

where

$$\widetilde{I}_{\text{e},1} = \frac{1}{J^{2/3}}\left(\operatorname{tr}\boldsymbol{C} - 2\gamma \boldsymbol{m}\cdot\boldsymbol{C}\boldsymbol{s} + \gamma^2 \boldsymbol{s}\cdot\boldsymbol{C}\boldsymbol{s}\right). \tag{32}$$

For a simple-shear test, the deformation gradient is described by a macroscopic applied shear λ such that

$$\boldsymbol{F} = \boldsymbol{I} + \lambda\, \boldsymbol{b}\otimes\boldsymbol{c}, \quad \boldsymbol{b}\cdot\boldsymbol{c} = 0, \quad |\boldsymbol{b}| = |\boldsymbol{c}| = 1. \tag{33}$$

We define the slip angle φ and shear angle θ for in-plane shearing and slip such that vectors $\boldsymbol{s}$, $\boldsymbol{m}$, $\boldsymbol{b}$ and $\boldsymbol{c}$ are given by

$$\boldsymbol{s} = \begin{pmatrix} \cos\varphi \\ \sin\varphi \\ 0 \end{pmatrix}, \qquad \boldsymbol{m} = \begin{pmatrix} -\sin\varphi \\ \cos\varphi \\ 0 \end{pmatrix}, \qquad \boldsymbol{b} = \begin{pmatrix} \cos\theta \\ \sin\theta \\ 0 \end{pmatrix}, \qquad \boldsymbol{c} = \begin{pmatrix} -\sin\theta \\ \cos\theta \\ 0 \end{pmatrix}. \tag{34}$$

For analytical simplicity, taking the special case of $\sigma^{\infty} \to 0$, we obtain a simplified form of the energy (which simplifies the hardening law and admits analytical treatment):

$$A(\gamma, \epsilon, \lambda) = \frac{1}{4}\left[\mu\left(\gamma^2(\lambda^2+2) + 2\lambda^2\right) + \gamma\lambda\mu\left[2(\lambda-\gamma)\sin\left(2(\theta-\varphi)\right) - (\gamma\lambda+4)\cos\left(2(\theta-\varphi)\right)\right] + 2H\epsilon^2\right]. \tag{35}$$

Note that for monotonous loading we have $\epsilon = |\gamma|$. For any choice of slip and shear angles satisfying $\varphi = \theta$, the energy thus simplifies to

$$A(\gamma, \lambda) = \frac{1}{2}\left[\mu(\gamma-\lambda)^2 + H\gamma^2\right]. \tag{36}$$

By minimizing with respect to the internal variable γ to obtain the minimizer $\gamma^*(\lambda)$, we analytically compute the condensed energy (Carstensen et al., 2002) as

$$A^*(\lambda) = \inf_{\gamma} A(\gamma, \lambda) = A\left(\lambda, \gamma^*(\lambda)\right) = \frac{H\lambda^2\mu}{2(H+\mu)} \qquad \forall \qquad H \neq -\mu. \tag{37}$$

It is obvious that for any physically reasonable range of shear modulus μ and hardening parameter H, this condensed energy density is quadratic and therefore convex. This implies that, if an RVE with slip angle φ is subject to shear such that $\varphi = \theta$, it will deform homogeneously throughout the applied loading.

By contrast, this is not the case when considering the space of all possible orientations (φ, θ) such that $\varphi \neq \theta$. For example, taking the case of slip and shear angles $\varphi = -\pi/3$ and $\theta = \pi/12$ and, once again, only considering monotonous loading, the energy reduces to

$$A(\gamma, \lambda) = \frac{1}{8}\left[2\gamma\lambda\left(\lambda + 2\sqrt{3}\right)\mu + \gamma^2\left(4H + \left[\lambda\left(\left(\sqrt{3}+2\right)\lambda - 2\right) + 4\right]\mu\right) + 4\lambda^2\mu\right]. \tag{38}$$

Minimization with respect to the slip γ yields the condensed energy density (Carstensen et al., 2002),

$$A^*(\lambda) = \frac{16H\lambda^2\mu + 7\lambda^4\mu^2 + 4\sqrt{3}\lambda^4\mu^2 - 4\sqrt{3}\lambda^3\mu^2 - 8\lambda^3\mu^2 + 4\lambda^2\mu^2}{8\left(4H + 2\lambda^2\mu + \sqrt{3}\lambda^2\mu - 2\lambda\mu + 4\mu\right)} \tag{39}$$

which holds for all

$$\lambda > 0 \quad \wedge \quad H > \frac{1}{4}\left[-\left(3\sqrt{3}+6\right)\lambda^2 + 6\lambda - 12\right]. \tag{40}$$

The condensed energy (39) is nonconvex in λ for a particular range of values in (H, λ)-space. For example, Fig. 1 plots the condensed energy (39) as a function of the loading parameter λ for various different hardening parameters H at fixed $\mu = 3$.

As the hardening parameter H decreases, the energy landscape becomes increasingly nonconvex, which implies that the energy can be lowered by the formation of microstructure, i.e., by breaking up the homogeneous deformation into heterogeneous domains or microstructural patterns (Klusemann and Kochmann, 2014). Previous analytical studies often used laminate constructions to approximate the rank-one-convex (and thus the quasiconvex) hull; see, e.g., Ortiz and Repetto (1999); Miehe et al. (2004); Kochmann and Hackl (2011). Here, we aim to calculate the energy-minimizing patterns by applying the spectral technique outlined in Section 3 to a single-crystal RVE. For a fair comparison between analytical solutions and numerical results, we seek energy-minimizing microstructures irrespective of loading history (i.e., we use a dissipation-free kinetic model) with the same parameters as the analytical model (using $H = 2.0 \cdot 10^{-4}$, $\mu = 3$, $\kappa = 3$, $\varphi = -\pi/3$, and $\theta = \pi/12$; note that the magnitude of the moduli does not affect the microstructure, so they are given in arbitrary units). We note that this dissipation-free example serves to illustrate energy-minimizing pattern formation, whereas later polycrystal Mg simulations will account for the dissipative effects of viscoplasticity.

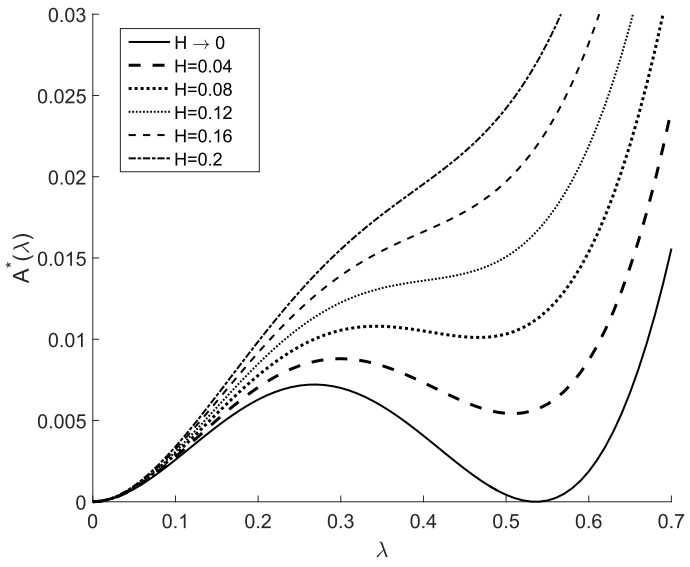

Figure 1: Loss of convexity of the condensed energy $A^*(\lambda)$ as the hardening parameter H decreases, for $\varphi = -\pi/3$ and $\theta = \pi/12$.

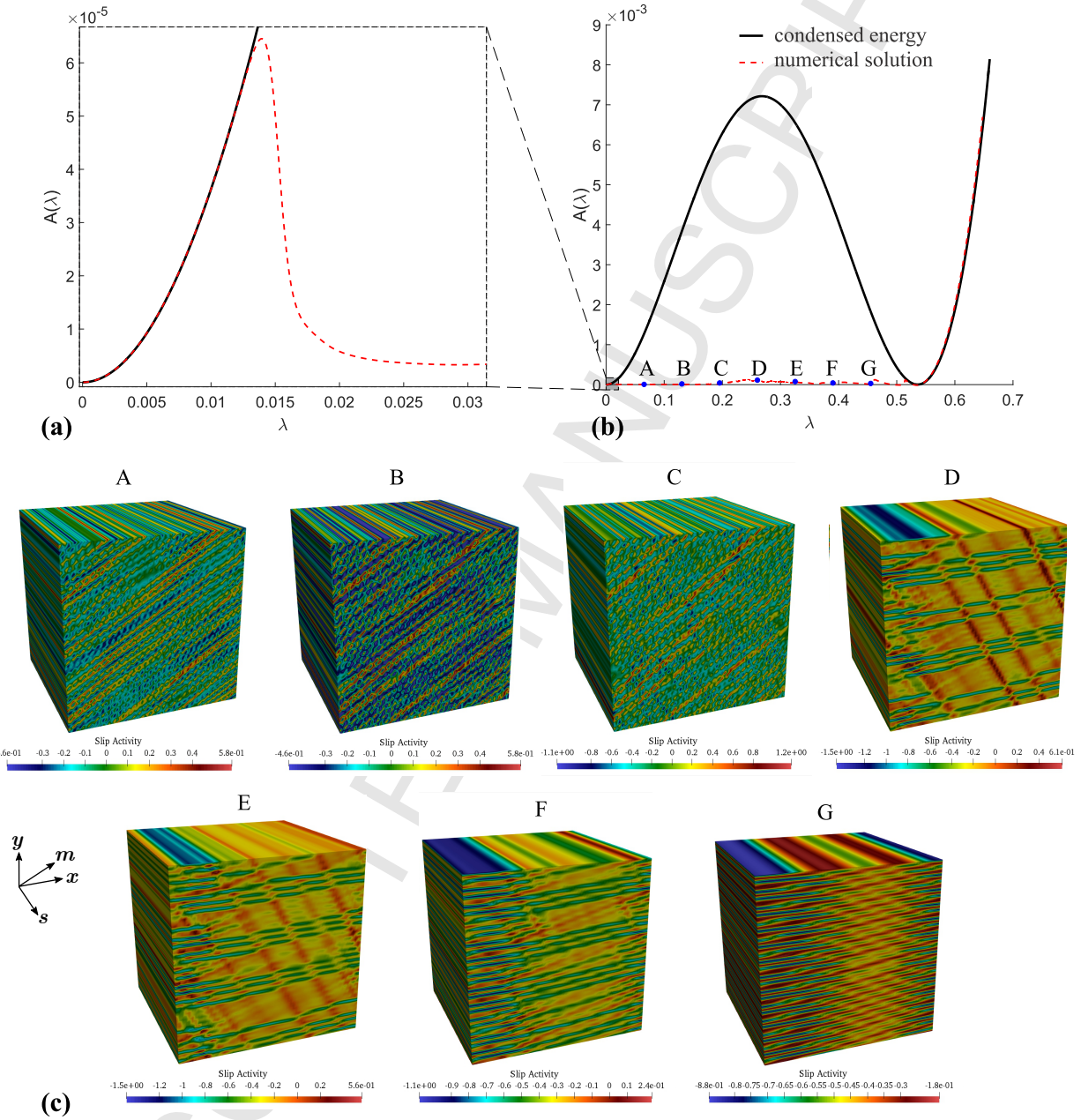

Figure 2: Approximation of the quasiconvex envelope obtained by spectral homogenization without finite-different approximation: the average energy of the RVE is compared to the non-convex condensed energy with (a) showing a magnification of (b); (c) shows the microstructural slip activity within the RVE at stages A through G along the loading path as indicated in (b).

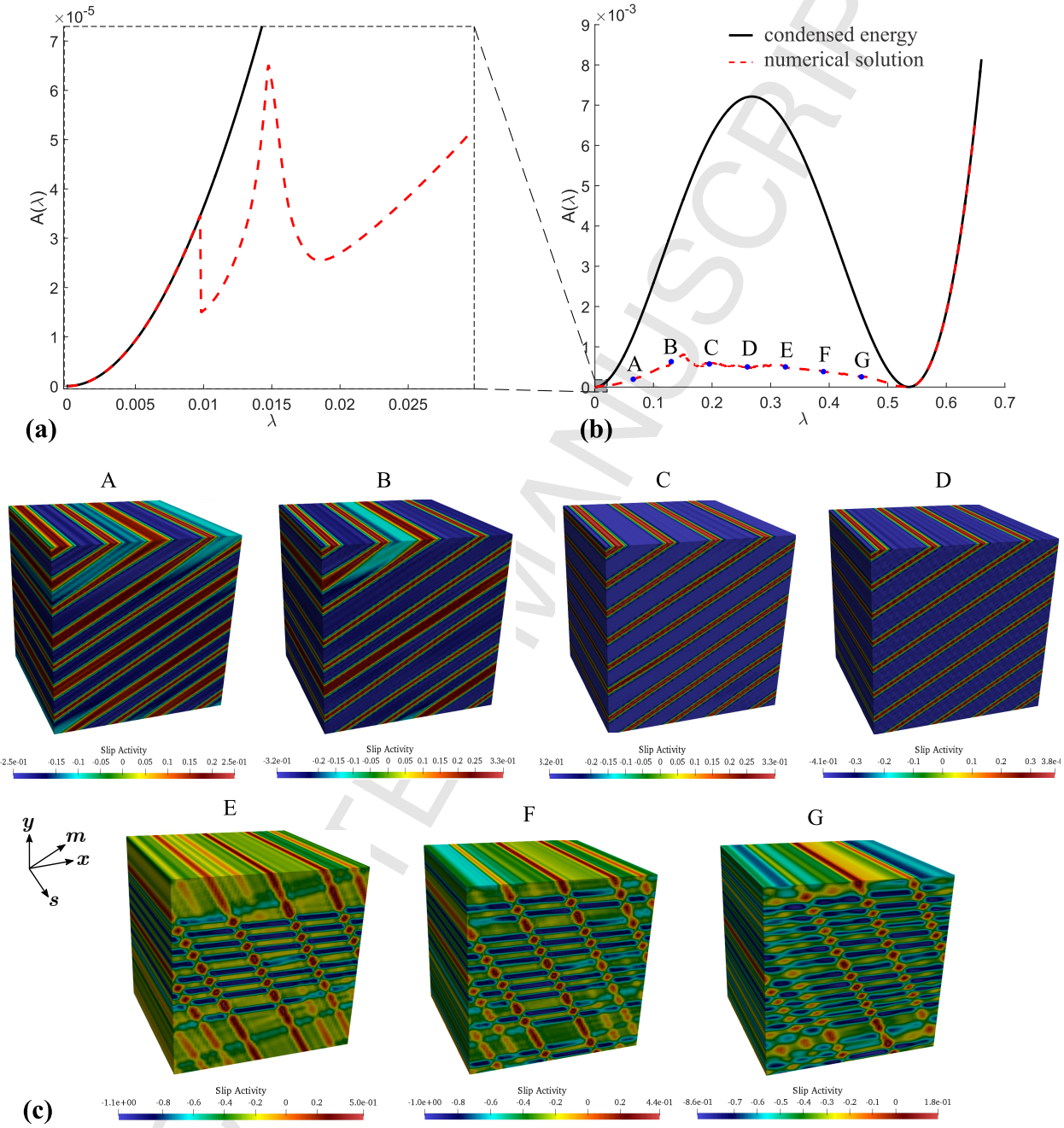

Figure 3: Approximation of the quasiconvex envelope obtained by spectral homogenization with the twelfth-order finite-difference approximation defined in (20): the average energy of the RVE is compared to the non-convex condensed energy with (a) showing a magnification of (b); (c) shows the microstructural slip activity within the RVE at stages A through G along the loading path as indicated in (b).

We begin by considering the standard spectral method without finite-difference smoothing and plot the relevant energies and slip activity in the reference configuration in Fig. 2. While the analytical solution of the quasiconvex hull corresponds to a laminate having zero strain energy between the two energy wells (Kochmann and Hackl, 2011), the numerical approximation is non-zero and experiences a series of jumps along the loading path, corresponding to sudden changes in microstructure. The initial state equilibrates into checkerboard-like patterns, followed by the gradual formation of transient laminate patterns that evolve with increasing load. Macro-laminates emerge at larger loads, displaying characteristics of first-, second- and higher-order laminates. However, due to the lack of a characteristic length scale, the observation of clean laminate patterns is rare and the numerical approximation of the quasiconvex hull produces complex, generally non-laminate patterns.

Like analytical lamination schemes (Ortiz and Repetto, 1999; Miehe et al., 2004; Kochmann and Hackl, 2011), the model whose results are shown in Fig. 2 neglects interface energies and therefore does not have an intrinsic length scale (in theory this results in infinitely fine infimizing sequences). In our numerical setting, interfaces between laminate domains contribute energy only when the finite-difference smoothing described in Section 3.3 is applied. Therefore, we proceed to repeat the simulation of Fig. 2 now with the modified Fourier transform of Section 3.3, which introduces an artificial, regularizing contribution to the stored energy, cf. (28). The analogous results are presented in Fig. 3. Both first- and second-order laminate patterns are observed, and the patterns are considerably cleaner than those without finite-difference regularization. It is also apparent that the finite-difference regularization results in thicker interfaces with a characteristic relative length scale; these regions, in turn, produce a diffuse interface-type contribution to the energy. Consequently, the path followed by the approximated quasiconvex hull is farther from the theoretical (zero-energy) envelope.

4.2. Interface energy and equivalent laminate microstructure

Laminate patterns as energy minimizers have a classical origin in the context of energy relaxation. Microstructural patterns are associated with the energy's quasiconvex hull (Morrey, 1952), which is hard to compute and therefore oftentimes estimated by upper and lower bounds, including the rank-one-convex hull Ortiz and Repetto (1999); Miehe et al. (2004); Kochmann and Hackl (2011). The latter emerges, e.g., from recursive lamination (Aubry et al., 2003), which assumes sharp interfaces (as opposed to the diffuse interfaces shown here) and constructs laminates by enforcing kinematic compatibility. For example, a first-order laminate can be constructed as an approximation of the rank-one-convex hull of the nonconvex energy density A, defining

$$R_1A(\boldsymbol{F}) = \inf\left\{ \nu_1 A(\boldsymbol{F}_1,\gamma_1) + \nu_2 A(\boldsymbol{F}_2,\gamma_2) \,|\, \nu_i, F_i : 0 \le \nu_i \le 1, \sum_i^n \nu_i = 1,\ \sum_i^n \nu_i \boldsymbol{F}_i = \boldsymbol{F},\ \mathrm{rank}(\boldsymbol{F}_1 - \boldsymbol{F}_2) \le 1 \right\}, \quad (41)$$

where ν_i denotes the volume fraction of laminate phases $i = 1,2$. In order to satisfy the Hadamard compatibility constraint, it is required that $\boldsymbol{F}_2 - \boldsymbol{F}_1 = \boldsymbol{a} \otimes \boldsymbol{N}$, with $\boldsymbol{N}$ being normal to the laminate interfaces and $\boldsymbol{a}$ being the projected amplitude of jump in deformation gradient across the interface. As discussed above, in the nonconvex region of the above example in the absence of hardening one obtains, e.g., $R_1A(\boldsymbol{F}) = 0$.

As an example, numerical results obtained from our diffuse-interface model and an equivalent sharp-interface laminate for the same simple shear test of Fig. 3 at an applied shear of $\lambda = 0.208$ are compared in Fig. 4 (a) and (b). From the simulated RVE solution, we can determine average quantities for each of the two laminate phases[2], evaluating to

$$\begin{aligned} \boldsymbol{F}_{\mathrm{e},1} &\approx \begin{pmatrix} 0.956 & -0.291 & 0 \\ 0.291 & 0.956 & 0 \\ 0 & 0 & 1 \end{pmatrix}, \qquad \boldsymbol{F}_{\mathrm{e},2} \approx \begin{pmatrix} 0.933 & 0.358 & 0 \\ -0.358 & 0.933 & 0 \\ 0 & 0 & 1 \end{pmatrix}, \qquad \gamma_1 \approx 0.312, \qquad \gamma_2 \approx -0.357, \\ \boldsymbol{a} &\approx \begin{pmatrix} 0.581 \\ 0.308 \\ 0 \end{pmatrix}, \qquad \boldsymbol{N} \approx \begin{pmatrix} 0.480 \\ -0.877 \\ 0 \end{pmatrix}, \qquad \theta \approx 28.7^\circ, \qquad \text{and} \qquad \nu_1 \approx 0.0993, \end{aligned} \quad (42)$$

[2]Histograms of slip activity for any given loading reveal the presence of two clear Gaussian peaks. The shown values for each of the two domains within the microstructural laminate pattern were thus obtained statistically from the mean of the Gaussians after thresholding.

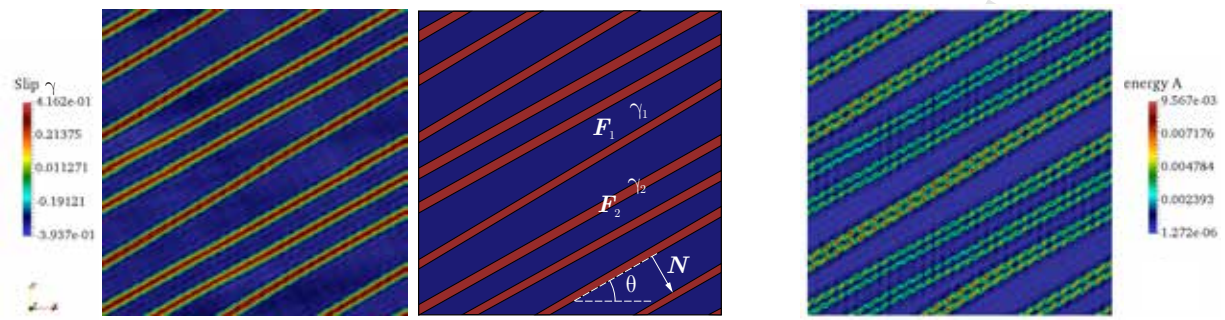

(a) **(b)** **(c)**

Figure 4: Laminate patterns for the simple shear test case at $\lambda = 0.208$ obtained from (a) numerical simulations using the above spectral homogenization framework and (b) the equivalent sharp-interface description. (c) shows the local energy density distribution of the numerical solution in (a), which shows concentrated energy within interfaces.

where θ denotes the laminate orientation with $\boldsymbol{N} = (\sin\theta, -\cos\theta, 0)^{\mathrm{T}}$; see Fig. 4(b). The corresponding sharp-interface energy is

$$A_{\text{laminate}} = \nu_1 A_1 + (1-\nu_1)A_2 = 1.61 \cdot 10^{-5}, \tag{43}$$

which is not zero (as in the ideal case of a sharp-interface laminate in this example) but significantly less than the condensed energy for homogeneous deformation at the same applied shear ($\lambda = 0.208$), which is $A^* = 6.49 \cdot 10^{-3}$ with

$$\gamma = -\frac{3\left(\lambda^2 + 2\sqrt{3}\lambda\right)}{4H + 3\sqrt{3}\lambda^2 + 6\lambda^2 - 6\lambda + 12} = -0.204 \quad \text{and} \quad F_{\text{e}} = \begin{pmatrix} 1.00 & 0.225 & 0 \\ -0.176 & 0.958 & 0 \\ 0 & 0 & 1 \end{pmatrix}. \tag{44}$$

Note that the above value of A_{laminate} is also considerably lower than the energy reported at point C in Fig. 3(b). This is because, due to the spectral regularization, the diffuse interfaces contribute additional energy, which raises the energy of the system as seen in the numerical simulation with $A_{\text{RVE}} = 5.66 \cdot 10^{-4}$ (point C in Fig. 3). Therefore, interface energy is significant and the reason for the higher energy path followed by the numerical solution with spectral regularization. This is confirmed by a plot of the local energy density in Fig. 4(c), showing an increased energy localized within the diffuse interfaces.

4.3. Extension to bicrystals

The above laminate microstructures are expected to emerge in infinite, periodic crystals, neglecting the abundance of defects at the mesoscale of metals. As a first step towards a polycrystal, we consider a bicrystal made of two perfectly-bonded grains separated by a sharp interface, each grain undergoing single-slip on their respective slip system. The effect on the energy of changing the misorientation while keeping the other parameters fixed is shown in Fig. 5 (using $H = 2.0 \cdot 10^{-4}$, $\mu = 3$, and $\theta = \pi/12$). We assign two different slip system orientations to the two grains of the bicrystal and apply a macroscopic simple shear deformation (using the same finite-difference correction outlined in Section 4, which provides a relative length scale as discussed above).

While each crystal would produce periodic laminate patterns as shown in the previous section, the bicrystal shows more interesting microstructural features. If loaded separately, each grain would reduce its energy by forming independent laminates whose orientations depend on the slip system orientation. When fused together in a bicrystal, compatibility across the interface imposes constraints, which affects the emerging microstructural patterns, as shown in Fig. 6. As the misorientation between the two grains increases (here, varying φ_2 from $-\pi/4$ to $-\pi/12$ while keeping φ_1 constant), laminates are suppressed in the central grain. As can be expected, low misorientation results in microstructural patterns spreading across grain boundaries and into adjacent grains. However, increasing the misorientation leads to the suppression of such patterns. We conclude that the presence of compatibility constraints significantly restricts the formation of energy-minimizing patterns within grains and results in a more complex picture, dependent on the misorientation and shape of grain boundaries. We may expect that this effect is dramatically more pronounced

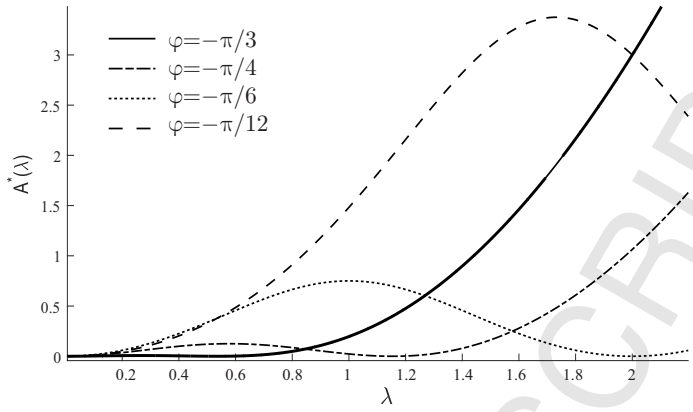

Figure 5: Influence of the slip system orientation φ on the non-convex, condensed energy landscape of a single-crystal, with all shown energies exhibiting non-convexity at different range of values for the shear parameter λ.

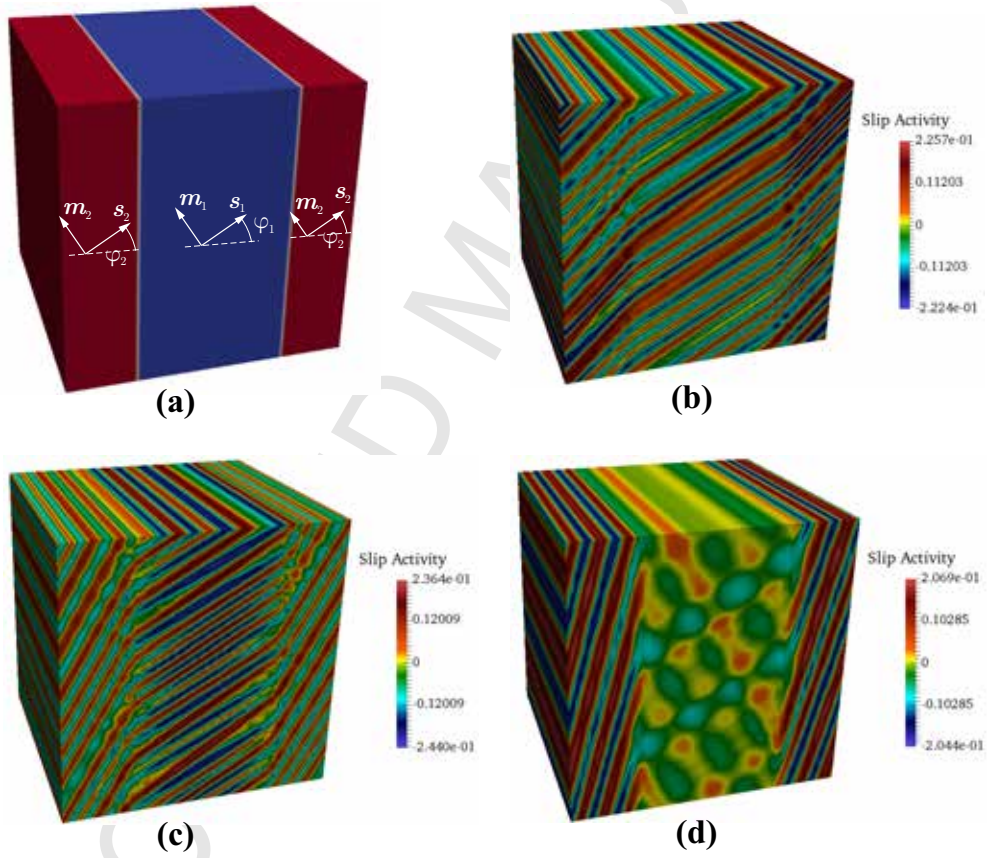

Figure 6: Laminate pattern formation in bicrystals at an applied shear strain of $\lambda = 0.03$: (a) the geometric arrangement of the two grains within the bicrystal RVE along with the definition of angles φ_1 and φ_2 in the blue and red grains, respectively. Results are shown for (b) $\varphi_1 = -\pi/3$ and $\varphi_2 = -\pi/4$, (c) $\varphi_1 = -\pi/3$ and $\varphi_2 = -\pi/6$, and (d) $\varphi_1 = -\pi/3$ and $\varphi_2 = -\pi/12$.

in polycrystals with abundant grain boundaries (GBs), such as those discussed in the next section. Therefore, polycrystals are anticipated to form more general patterns (not necessarily clean laminates) but such patterns may emerge due to the non-(quasi)convexity of the energy.

5. Plasticity in polycrystalline magnesium

Having shown how our spectral homogenization scheme predicts microstructure formation in finite-strain crystal plasticity, we proceed to apply the same techniques to polycrystals of Mg described by the constitutive model of Section 2. The material and numerical parameters used in this section are listed in Appendix B. We study polycrystalline representative volume elements (RVEs) whose effective response is obtained from homogenization with periodic boundary conditions, using the spectral scheme of Section 3. Periodic polycrystals with a specified number of grains are generated using the open-source package Neper as described by Quey et al. (2011). Grain orientations are assigned with random permutations such that the overall texture matches the shown pole figures. The spectral scheme admits sufficient grid resolution to capture large numbers of grains, which is why we use this setup to investigate the relation between microstructural details and the effective response. In Section 5.1, RVEs are subjected to simple shear loading, and effective stress-strain responses together with spatial distributions of inelastic activity are shown. Additionally, the influence of increasing grain misorientation (i.e., increasing the spread of the texture pole) on the effective macro- and meso-scale behavior is analyzed. Subsequently, in Section 5.2 polycrystals undergo combined compressive/shear loading to mimic the effects of cold rolling. Here, we particularly study the influence of the number of grains per RVE (for approximately constant texture) on the effective macroscale stress-strain response.

5.1. Simple shear and the influence of texture

We subject polycrystalline RVEs containing 100 grains to simple shear loading with an average deformation gradient

$$\boldsymbol{F}^0 = \begin{pmatrix} 1 & \lambda & 0 \\ 0 & 1 & 0 \\ 0 & 0 & 1 \end{pmatrix}, \tag{45}$$

where λ is raised from 0 to 10% at a rate of $\dot{\lambda} = 0.02\ \mathrm{s}^{-1}$. The chosen texture, representative of extruded Mg (Chang et al., 2017), is shown in the pole figure in Fig. 7(b). The resulting effective stress-strain relation is illustrated in Fig. 7(a) and exhibits a plateau near $P_{12} = 0.1$ GPa at $\lambda \approx 0.05$, caused by stress relaxation due to slip and twinning mechanisms across grains. The emergence of heterogeneous stresses and inelastic activity within grains and stress concentrations at grain boundaries, even at low texture and therefore low grain-to-grain misorientations, is observed. In particular, twinning is initiated primarily at triple junctions as seen in the total twin activity shown in Fig. 7(c), which also visualizes how the texture distribution results in only a subset of all grains exhibiting deformation twinning by extension twins. In particular the total volume fraction of the $\langle \bar{1}012 \rangle$ extension twins increases to a maximum of 0.183 and the activity on $\langle 11\bar{2}0 \rangle$ prismatic slip systems to 0.0974 during the deformation at $\lambda = 0.09$.

To gain quantitative insight into how increasing the grain misorientation affects the effective material response, the RVE is endowed with increasingly wider spread of texture and subjected to the same shear loading parametrized by (45). We note that texture strength and grain-to-grain misorientations are not directly correlated but, in case of sufficiently many grains and a random assignment of grain orientations, the two are assumed to correlate. In Fig. 8(a) the resulting effective stress-strain responses for different textures indicate an increasingly softer response with increasing texture, even at low strains of around $\lambda = 0.01$, which is indicative of the anisotropy of slip-twin interactions. The spreading of the texture pole leads to the activation of more slip and twin systems across a wider range of grains, leading to a softer response but also stronger stress gradients and concentrations particularly near grain boundaries, see Fig. 8(c). The stress-strain curves indicate that decreasing the texture leads to a slightly lower yield stress but a significantly higher hardening: at higher strains of, e.g., $\lambda = 0.01$, there is a deviation in the shear stress of $\Delta P_{12} \approx 36\%$ between the extremal cases of texture cases (A) and (E) in Fig. 8. The increased number of inelastic-strain-accommodating slip planes and twin systems in highly textured polycrystals such as case (E) induces stress relaxation, which in turn results in the observed changes in hardening. For instance, at $\lambda = 0.01$, for case (A) the peak total twin activity is 0.105, whereas for case (E) it is 0.252. Similarly, the maximal basal slip activity for case (A) is 0.0177, while that of case (E) is 0.0797. Notice how several of the grains display pattern-like stress and slip/twin distributions; the effect is much less pronounced than in the single-crystal case discussed before due to the abundance of available twin/slip mechanisms. However, there are still individual grains demonstrating energy-minimizing microstructural pattern formation, as highlighted in Fig 9.

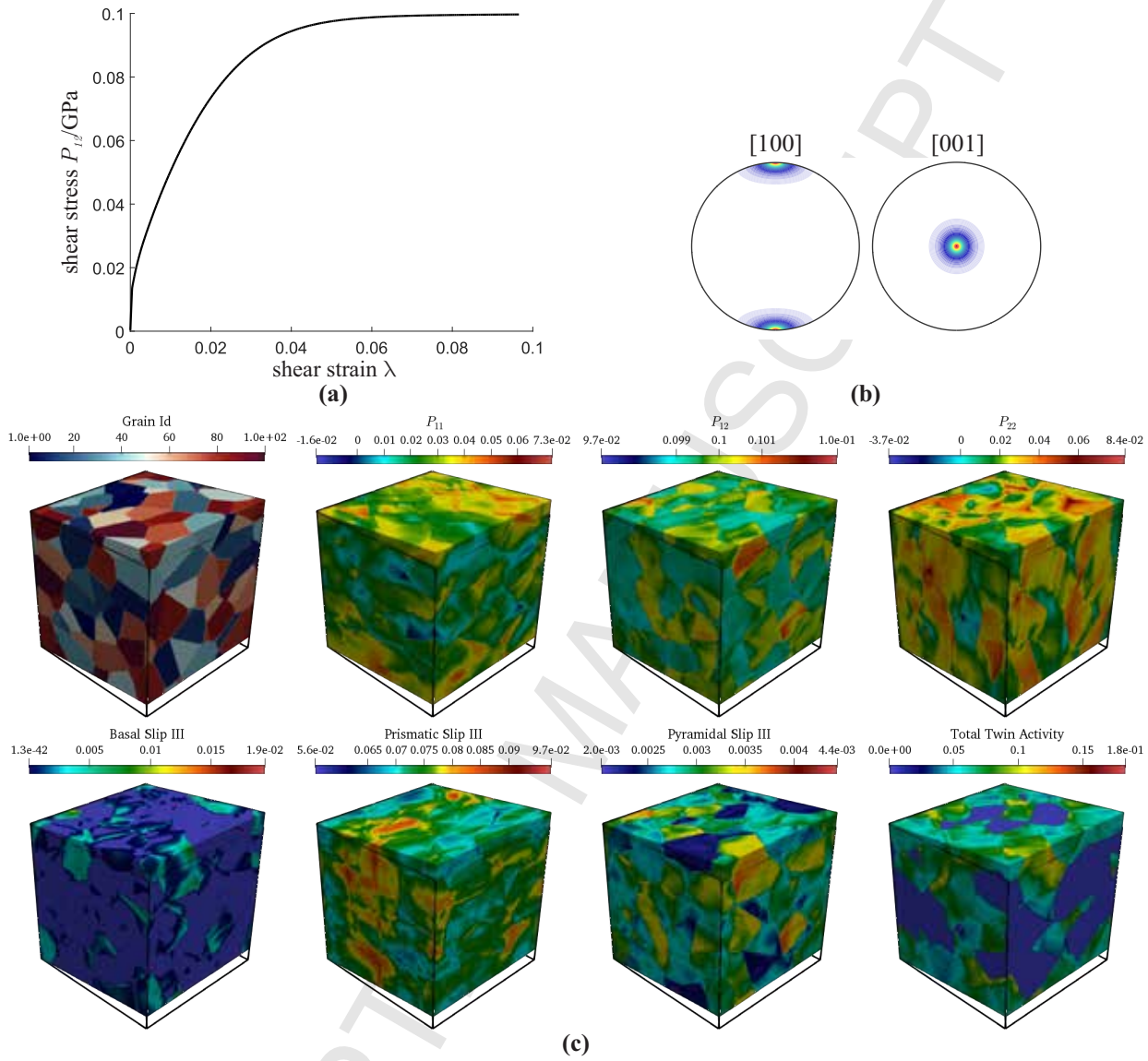

Figure 7: (a) Effective stress-strain response of a simple shear test of an RVE containing 100 grains whose orientations are shown in the pole figure (b). (c) State of the RVE at an applied average shear strain of $F^0_{12} = \lambda = 0.09$. RVEs are shown in the deformed configuration, whereas the bounding box indicates the undeformed shape. Plots illustrate the grain shapes, components of the first Piola-Kirchhoff stress tensor $\boldsymbol{P}$ as well as the distribution of prismatic slip and of the total volume fraction of all extension-twinned regions. The shown stress distributions are in units of GPa.

5.2. Cold rolling and the influence of the number of grains

Having a computational model and toolset at hand to simulate the RVE response with high resolution, the question arises as to what level of microstructural detail is required to predict the effective, macroscopic stress-strain response. As an example test case, we choose the cold rolling process which is classically modeled as a combination of shear and compression; see, e.g., (Lee and Duggan, 1991; Ahzi et al., 1993). For ease of implementation, we here take a

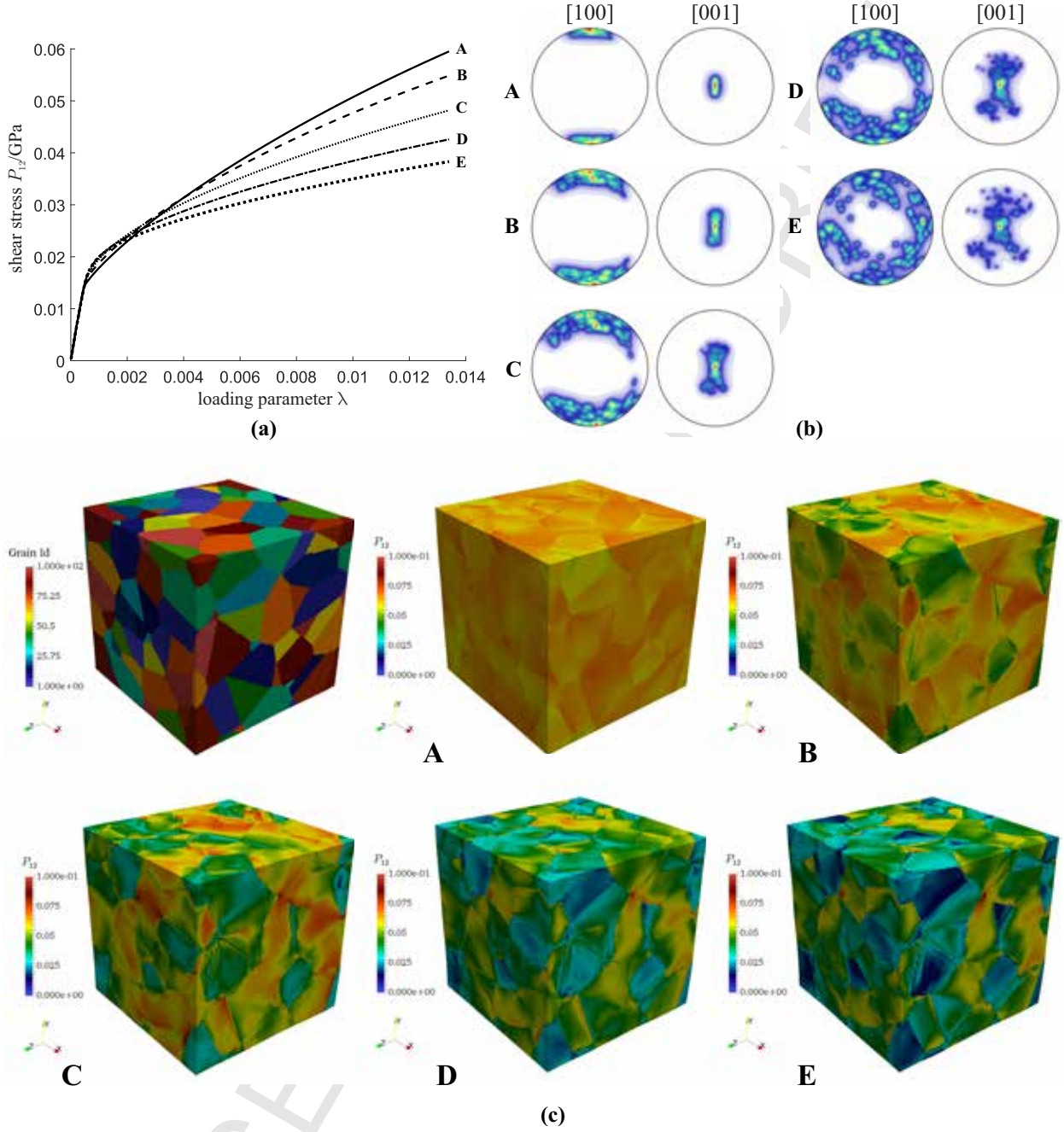

Figure 8: Using the same grain geometry as in Fig. 7(a), we investigate how the effective stress-strain response in (a) changes with increasing texture, as shown by the pole figures in (b). Increasing the spread of the texture allows more easy-slip and -twin systems to become active across a larger number of grains, resulting in significant softening even at low strains. (c) The resulting shear stress distribution illustrates stronger stress differences and concentrations with increasing texture spread. The shown stress distributions are in units of GPa.

deformation history described by the effective isochoric deformation gradient

$$\boldsymbol{F}^0 = \begin{pmatrix} 1+\frac{\lambda}{3} & 0 & \lambda \\ 0 & 1 & 0 \\ 0 & 0 & \frac{3}{3+\lambda} \end{pmatrix} \tag{46}$$

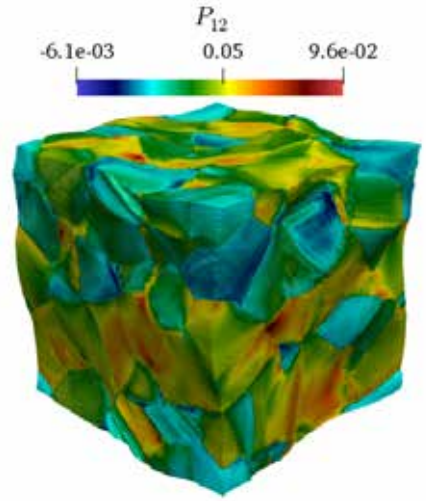

Figure 9: Polycrystalline case (E) of the simple shear experiment (see the pole figure in Fig. 8): shown is the shear stress distribution (in GPa) with all displacements magnified by a factor of 10 for better visibility. Several of the grains display laminate-like patterns, as may be expected due to the non-quasiconvexity in finite-strain crystal plasticity, as discussed above.

with loading parameter $\lambda \geq 0$. We simulate the effective response of four different RVEs, containing 20, 50, 100, and 1000 grains. All grain orientations were generated randomly from the same pole figure, viz. case C from Fig. 8(b). Since this does not produce a unique assignment of orientations to grains, we consider the statistics and simulate an ensemble of ten RVE realizations for each number of grains (i.e., the ten realizations for a given grain geometry differ by the permutation of grain orientations while keeping the same set of orientations from the pole figure). This yields an envelope of stress-strain responses summarized in Fig. 10, showing the mean and standard deviation for each of the four different RVEs studied. As expected, the envelope of possible stress-strain responses (shown as the shaded region) is large when using only 20 grains, but we observe convergence towards a narrow stress-strain envelope as the number of grains within the RVE increases. Interestingly, but not entirely unexpected, there is also (non-monotonic) convergence of the mean stress-strain response shown by the solid lines in Fig. 10, where the curves vary only little between 20 and 1000 grains. In other words, while the envelope of possible stress-strain responses is large for an RVE with a relatively small number of grains (e.g., 20), the mean response over many possible geometric permutations and sampling sequences reproduces approximately the same effective material response as an RVE with many more grains (e.g., 1000). Fig. 11 demonstrates representative stress states within the four different polycrystals at $\lambda = 0.01$, visualizing the effect of homogenizing the effective material response across increasing numbers of grains.

Overall, these results demonstrate that, although our high-resolution spectral scheme admits high-fidelity simulations of mesoscale slip and twin mechanisms, the effective stress-strain response as obtained from homogenization does not require highest levels of mesoscale resolution but may be approximated sufficiently well with small numbers of grains inside an RVE. Obtaining the mean response over a large number of RVE realizations, together with periodic boundary conditions, converges to an effective constitutive behavior. Of course, the converged response and the convergence behavior depend on the chosen material model and the geometric complexity (and we cannot draw general conclusions from the particular examples shown here), but the above examples with the chosen finite-strain crystal plasticity model, including slip and twinning as well as diffuse interfaces due to non-convex pattern formation in geometrically complex polycrystals, confirm this observation.

Finally, we verify the influence of the order of the finite-difference approximation on the obtained polycrstyalline results. To this end, Fig. 12 summarizes the stress–strain response for a simple-shear test of an RVE containing 100 grains. As expected, deviations are moderate and the effective response converges quickly towards the solution obtained from the uncorrected, standard Fourier spectral method when increasing the order of the finite-difference stencil. Fig. 13 illustrates the corresponding local fields (shown are two representative stress components as well as the total basal slip activity and the total twin activity). Again as expected, the standard scheme reveals oscillations in the local fields (corrupting convergence with h-refinement), which are removed by the finite-difference-approximated

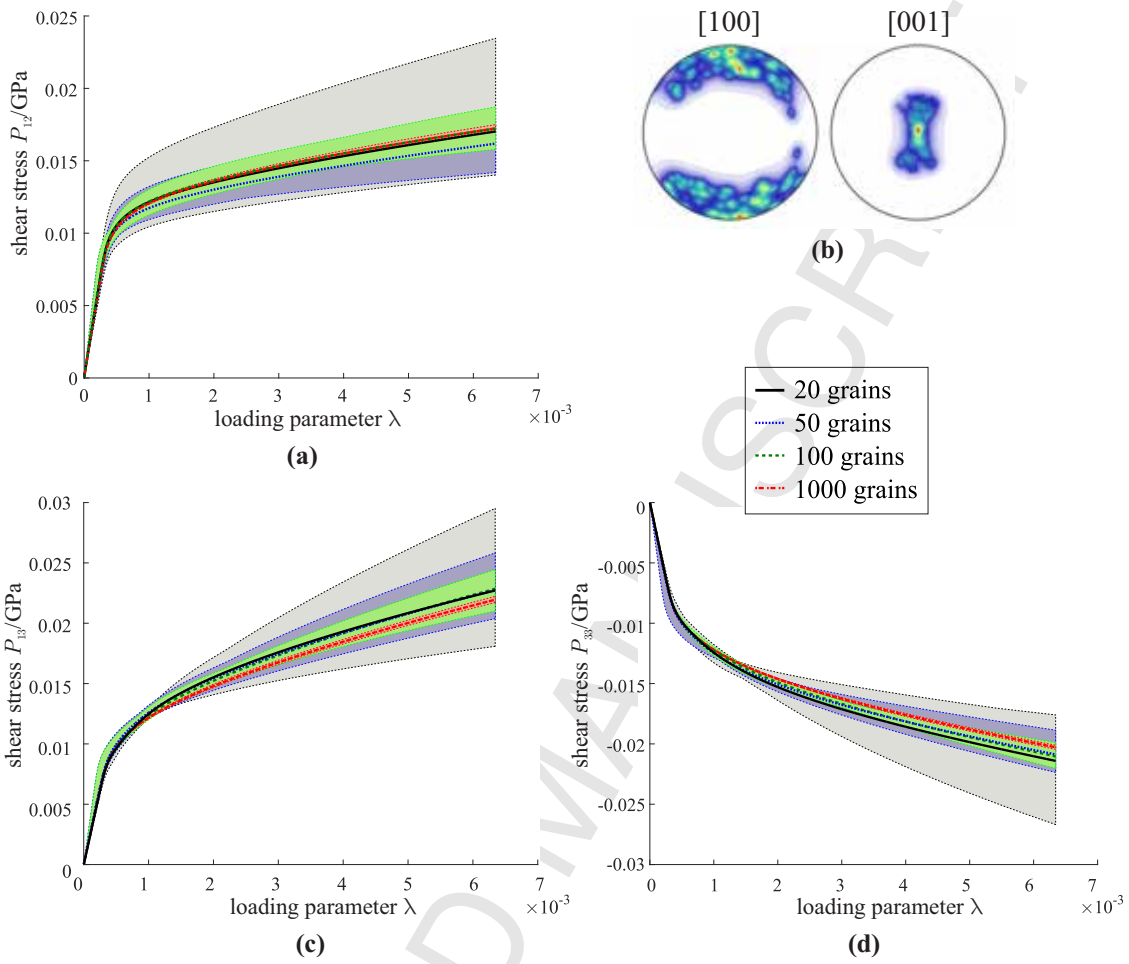

Figure 10: Influence of permuting the grain orientations within an RVE with fixed grain geometry: stress-strain behavior shown in terms of mean and standard deviation of ten RVE realizations with different permutations of grain-orientation assignments for RVEs containing 20, 50, 100, and 1000 grains. Grain orientations are taken from the pole shown in (b); the given components of the first Piola-Kirchhoff stress tensor include (a) tensile, (c) shear, and (d) compressive stresses. Mean stresses are shown as thick lines, standard deviations as shaded color regions.

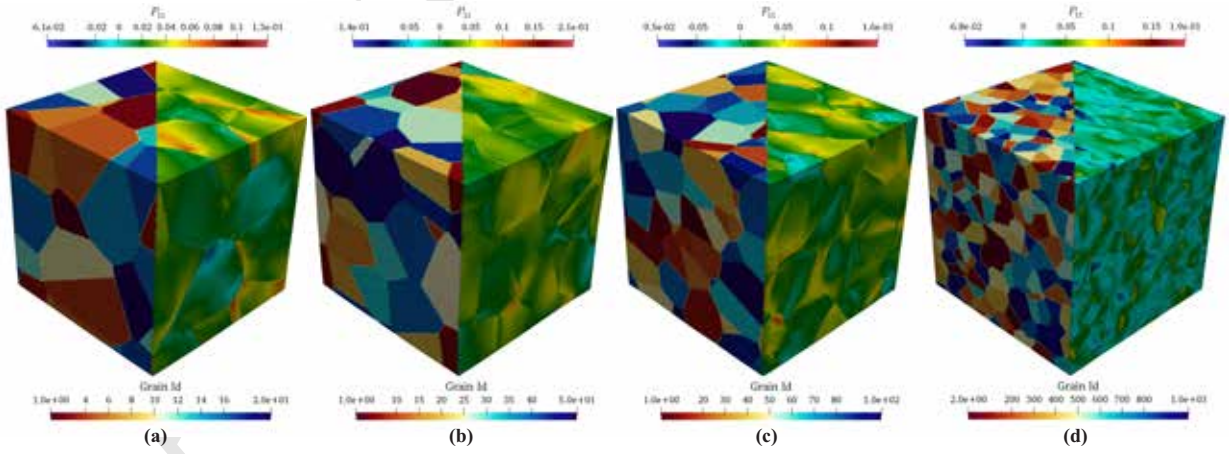

Figure 11: Polycrystalline RVEs with (a) 20, (b) 50, (c) 100, and (d) 1000 grains. The left half of each graphic illustrates the grain size and arrangement, whereas the right half shows the tensile/compressive stress distribution at a representative load of $\lambda = 0.01$.

schemes – where increasing the finite-difference order again leads to convergence towards the standard scheme.

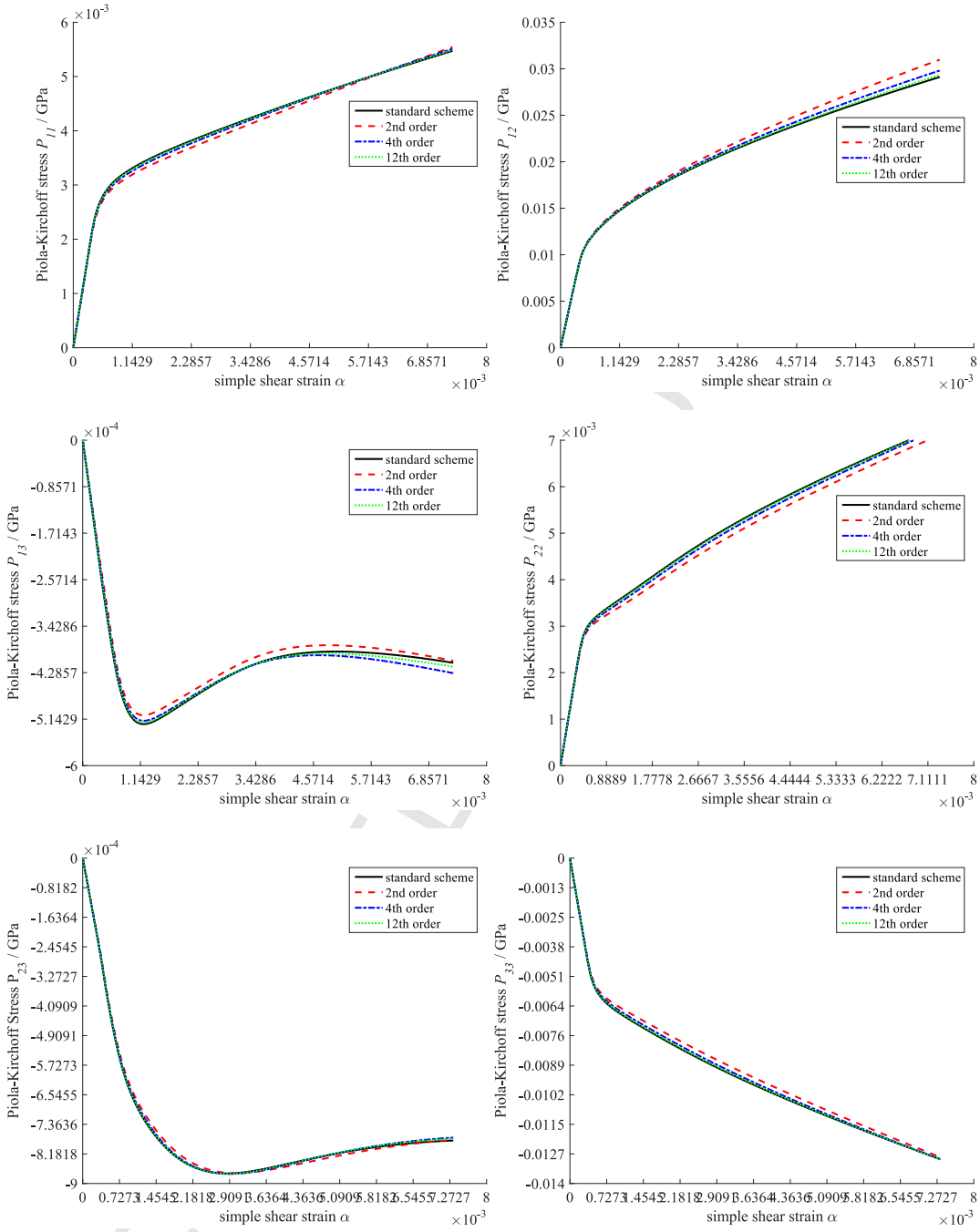

Figure 12: Illustration of the stress–strain response for simple shear loading ($F^0_{12} = \alpha$) showing convergence with increasing order of the finite-difference approximation to the standard Fourier spectral scheme.

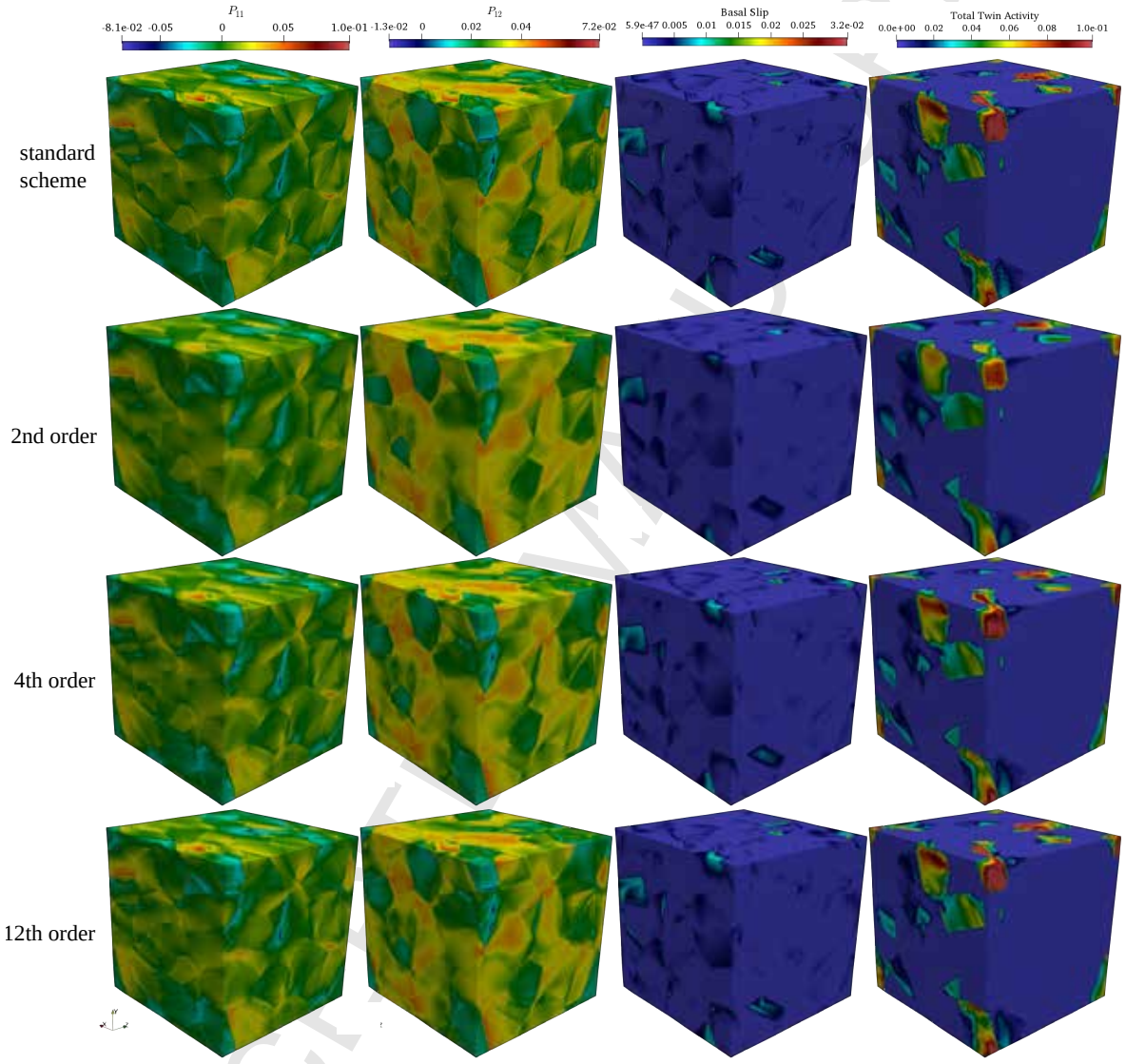

Figure 13: Illustration of the local stress fields and inelastic activity within the same RVE, obtained with different orders of the finite-difference approximation, shown at the maximum shear strain shown in Fig. 12.

6. Conclusions

We have discussed how a finite-difference-corrected spectral homogenization scheme along with an extended crystal plasticity model can describe the effective, macroscale response of polycrystalline pure Mg. We have shown that the improved Fourier spectral scheme for periodic homogenization introduces a regularization and an associated relative length scale that stabilizes microstructural patterns within the RVE. For single- and bicrystals deforming in single-slip we have demonstrated the emergence of laminate patterns and contrasted simulated RVE results with classical lamination theory, showing good agreement (hence, the shown homogenization setup is suitable to estimate energy-minimizing patterns and the associated quasiconvexified energy density). When applied to polycrystalline Mg, we verified a strong influence of the initial texture on the effective stress-strain response, and we demonstrated the convergence of the effective material behavior with an increasing number of grains within the RVE (enabled by the high-resolution spectral formulation employed here). This final point demonstrates that, although high resolution can be achieved by the presented scheme, lower levels of microscale details may be sufficient to capture the effective stress-strain response through averaging over different RVE realizations.

Acknowledgment

This research was sponsored by the Army Research Laboratory and was accomplished under Cooperative Agreement Number W911NF-12-2-0022. The views and conclusions contained in this document are those of the authors and should not be interpreted as representing the official policies, either expressed or implied, of the Army Research Laboratory or the U.S. Government. The U.S. Government is authorized to reproduce and distribute reprints for Government purposes notwithstanding any copyright notation herein.

References

Agnew, S. R., Duygulu, Ö., 2005. Plastic anisotropy and the role of non-basal slip in magnesium alloy AZ31B. International Journal of Plasticity 21 (6), 1161–1193.

Ahzi, S., Asaro, R. J., Parks, D. M., 1993. Application of crystal plasticity theory for mechanically processed {BSCCO} superconductors. Mechanics of Materials 15 (3), 201 – 222.
URL http://www.sciencedirect.com/science/article/pii/016766369390018M

Aubry, S., Fago, M., Ortiz, M., 2003. A constrained sequential-lamination algorithm for the simulation of sub-grid microstructure in martensitic materials. Computer Methods in Applied Mechanics and Engineering 192 (26), 2823 – 2843.
URL http://www.sciencedirect.com/science/article/pii/S0045782503002603

Ball, J. M., 1977. Convexity Conditions and Existence Theorems in Nonlinear Elasticity. Archive of Rational Mechanics and Analysis 63, 337–403.

Ball, J. M., James, R. D., 1987. Fine phase mixtures as minimizers of energy. Archive for Rational Mechanics and Analysis 100 (1), 13–52.

Bartels, S., Carstensen, C., Conti, S., Hackl, K., Hoppe, U., Orlando, A., 2006. Relaxation and the Computation of Effective Energies and Microstructures in Solid Mechanics. Springer Berlin Heidelberg, Berlin, Heidelberg, pp. 197–224.
URL https://doi.org/10.1007/3-540-35657-6_8

Bartels, S., Carstensen, C., Hackl, K., Hoppe, U., 2004. Effective relaxation for microstructure simulations: Algorithms and applications. Computer Methods in Applied Mechanics and Engineering 193 (48-51), 5143–5175.

Bartels, S., Prohl, A., 2004. Multiscale resolution in the computation of crystalline microstructure. Numerische Mathematik 96 (4), 641–660.

Becker, R., Lloyd, J. T., 2016. A reduced-order crystal model for HCP metals: Application to Mg. Mechanics of Materials 98, 98–110.

Berbenni, S., Taupin, V., Djaka, K. S., Fressengeas, C., 2014. A numerical spectral approach for solving elasto-static field dislocation and g-disclination mechanics. International Journal of Solids and Structures 51 (23-24), 4157–4175.

Brenner, R., 2009. Numerical computation of the response of piezoelectric composites using Fourier transform. Physical Review B 79 (March), 184106.

Brisard, S., Dormieux, L., 2010. FFT-based methods for the mechanics of composites: A general variational framework. Computational Materials Science 49 (3), 663–671.

Brown, C. M., Dreyer, W., Müller, W. H., 2002. Discrete fourier transforms and their application to stressstrain problems in composite mechanics: a convergence study. In: Proceedings of the Royal Society of London A: Mathematical, Physical and Engineering Sciences. Vol. 458. The Royal Society, pp. 1967–1987.

Carstensen, C., Hackl, K., Mielke, A., 2002. Non–convex potentials and microstructures in finite–strain plasticity. Proceedings of the Royal Society of London A: Mathematical, Physical and Engineering Sciences 458 (2018), 299–317.
URL http://rspa.royalsocietypublishing.org/content/458/2018/299

Carstensen, C., Plecháč, P., 1997. Numerical solution of the scalar double-well problem allowing microstructure. Mathematics of Computation 66 (219), 997–1026.
URL http://www.ams.org/mcom/1997-66-219/S0025-5718-97-00849-1/

Chang, Y., Kochmann, D. M., 2015. A variational constitutive model for slip-twinning interactions in hcp metals : Application to single- and polycrystalline magnesium. International Journal of Plasticity, 1–23.
URL http://dx.doi.org/10.1016/j.ijplas.2015.03.008

Chang, Y., Lloyd, J. T., Becker, R., Kochmann, D. M., 2017. Modeling microstructure evolution in magnesium: Comparison of detailed and reduced-order kinematic models. Mechanics of Materials 108, 40–57.
URL http://dx.doi.org/10.1016/j.mechmat.2017.02.007

Cheng, J., Ghosh, S., 2017. Crystal plasticity finite element modeling of discrete twin evolution in polycrystalline magnesium. Journal of Mechanics and Physics of Solids 99 (July 2016), 512–538.

Clayton, J. D., Knap, J., 2011. A phase field model of deformation twinning: Nonlinear theory and numerical simulations. Physica D: Nonlinear Phenomena 240 (9-10), 841–858.
URL http://dx.doi.org/10.1016/j.physd.2010.12.012

Conti, S., Dolzmann, G., Klust, C., 2009. Relaxation of a class of variational models in crystal plasticity. Proceedings of the Royal Society A: Mathematical, Physical and Engineering Sciences 465 (2106), 1735–1742.
URL http://rspa.royalsocietypublishing.org/cgi/doi/10.1098/rspa.2008.0390

Conti, S., Ortiz, M., 2008. Minimum principles for the trajectories of systems governed by rate problems. Journal of the Mechanics and Physics of Solids 56 (5), 1885–1904.

Conti, S., Theil, F., Oct 2005. Single-slip elastoplastic microstructures. Archive for Rational Mechanics and Analysis 178 (1), 125–148.
URL https://doi.org/10.1007/s00205-005-0371-8

Dixit, N., Xie, K. Y., Hemker, K. J., Ramesh, K. T., 2015. Microstructural evolution of pure magnesium under high strain rate loading. Acta Materialia 87, 56–67.
URL http://dx.doi.org/10.1016/j.actamat.2014.12.030

Eisenlohr, P., Diehl, M., Lebensohn, R. A., Roters, F., 2013. A spectral method solution to crystal elasto-viscoplasticity at finite strains. International Journal of Plasticity 46, 37–53.
URL http://linkinghub.elsevier.com/retrieve/pii/S0749641912001428

Gibbs, J. W., 1898. Fourier's series. Nature 59, 200.
URL http://www.nature.com/nature/journal/v59/n1522/abs/059200b0.html

Gibbs, J. W., 1899. Fourier's series. Nature 59, 606.
URL http://www.nature.com/nature/journal/v59/n1539/pdf/059606a0.html

Graff, S., Brocks, W., Steglich, D., 2007. Yielding of magnesium: From single crystal to polycrystalline aggregates. International Journal of Plasticity 23 (12), 1957–1978.

Hackl, K., Fischer, F. D., 2008. On the relation between the principle of maximum dissipation and inelastic evolution given by dissipation potentials. Proceedings of the Royal Society A: Mathematical, Physical and Engineering Sciences 464 (2089), 117–132.
URL http://rspa.royalsocietypublishing.org/cgi/doi/10.1098/rspa.2007.0086

Hackl, K., Kochmann, D., 2008. Relaxed potentials and evolution equations for inelastic microstructures. In: Reddy, B. (Ed.), IUTAM Symposium on Theoretical, Computational and Modelling Aspects of Inelastic Media. Vol. 11 of IUTAM Bookseries. pp. 27–39.

Hewitt, E., Hewitt, R. E., 1979. The gibbs-wilbraham phenomenon: An episode in fourier analysis. Archive for History of Exact Sciences 21 (2), 129–160.
URL http://dx.doi.org/10.1007/BF00330404

Homayonifar, M., Mosler, J., 2011. On the coupling of plastic slip and deformation-induced twinning in magnesium: A variationally consistent approach based on energy minimization. International Journal of Plasticity 27 (7), 983–1003.
URL http://dx.doi.org/10.1016/j.ijplas.2010.10.009

Homayonifar, M., Mosler, J., 2012. Efficient modeling of microstructure evolution in magnesium by energy minimization. International Journal of Plasticity 28 (1), 1–20.
URL http://dx.doi.org/10.1016/j.ijplas.2011.05.011

Izadbakhsh, A., Inal, K., Mishra, R. K., Niewczas, M., 2011. New crystal plasticity constitutive model for large strain deformation in single crystals of magnesium. Computational Materials Science 50 (7), 2185–2202.

Kabel, M., Boehlke, T., Schneider, M., 2014. Efficient fixed point and Newton-Krylov solvers for FFT-based homogenization of elasticity at large deformations. Computational Mechanics 54 (6), 1497–1514.

Kalidindi, S. R., 2001. Modeling anisotropic strain hardening and deformation textures in low stacking fault energy fcc metals. International Journal of Plasticity 17 (6), 837–860.

Kelley, E. W., Hosford, W. F., 1968. The Deformation Characteristics of Textured Magnesium. Transactions Of The Metallurgical Society Of AIME 242 (April), 654 – 661.

Klusemann, B., Kochmann, D. M., 2014. Microstructural pattern formation in finite-deformation single-slip crystal plasticity under cyclic loading: Relaxation vs. gradient plasticity. Computer Methods in Applied Mechanics and Engineering 278, 765–793.
URL http://dx.doi.org/10.1016/j.cma.2014.05.015

Kochmann, D., Hackl, K., 2011. The evolution of laminates in finite crystal plasticity: a variational approach. Continuum Mechanics and Thermodynamics 23 (1), 63–85.
URL http://www.springerlink.com/content/b02h6085l620u737/?MUD=MP

Kochmann, J., Wulfinghoff, S., Ehle, L., Mayer, J., Svendsen, B., Reese, S., Sep 2017. Efficient and accurate two-scale fe-fft-based prediction of the effective material behavior of elasto-viscoplastic polycrystals. Computational Mechanics.
URL https://doi.org/10.1007/s00466-017-1476-2

Kochmann, J., Wulfinghoff, S., Reese, S., Mianroodi, J. R., Svendsen, B., 2016. Two-scale FE-FFT- and phase-field-based computational modeling of bulk microstructural evolution and macroscopic material behavior. Computer Methods in Applied Mechanics and Engineering 305, 89–110.
URL http://dx.doi.org/10.1016/j.cma.2016.03.001

Kurukuri, S., Worswick, M. J., Tari, D. G., Mishra, R. K., Carter, J. T., 2014. Rate sensitivity and tension compression asymmetry in AZ31B

magnesium alloy sheet. Phil. Trans. R. Soc. A 372, 1–16.
Lahellec, N., Michel, J.-C., Moulinec, H., Suquet, P., 2003. Analysis of inhomogeneous materials at large strains using fast fourier transforms. In: IUTAM symposium on computational mechanics of solid materials at large strains. Springer, pp. 247–258.
Lanczos, C., 1956. Applied Analysis. Van Nostrand, Princeton, NJ.
Lebensohn, R. A., Kanjarla, A. K., Eisenlohr, P., 2012. An elasto-viscoplastic formulation based on fast Fourier transforms for the prediction of micromechanical fields in polycrystalline materials. International Journal of Plasticity 32-33, 59–69.
URL http://dx.doi.org/10.1016/j.ijplas.2011.12.005
Lebensohn, R. A., Needleman, A., 2016. Numerical implementation of non-local polycrystal plasticity using fast fourier transforms. Journal of the Mechanics and Physics of Solids 97, 333 – 351, sI:Pierre Suquet Symposium.
URL http://www.sciencedirect.com/science/article/pii/S0022509616301958
Lee, C., Duggan, B., 1991. A simple theory for the development of inhomogeneous rolling textures. Metallurgical Transactions A 22 (11), 2637–2643.
URL http://dx.doi.org/10.1007/BF02851357
Máthis, K., Čapek, J., Zdražilová, Z., Trojanová, Z., 2011. Investigation of tension-compression asymmetry of magnesium by use of the acoustic emission technique. Materials Science and Engineering A 528 (18), 5904–5907.
Michel, J. C., Moulinec, H., Suquet, P., 2001. A computational scheme for linear and nonlinear composites with arbitrary phase contrast. International Journal for Numerical Methods in Engineering 52 (12), 139–160.
URL http://doi.wiley.com/10.1002/nme.275
Miehe, C., Lambrecht, M., Gürses, E., 2004. Analysis of material instabilities in inelastic solids by incremental energy minimization and relaxation methods: evolving deformation microstructures in finite plasticity. Journal of the Mechanics and Physics of Solids 52, 2725–2769.
Mishra, N., Vondrejc, J., Zeman, J., 2015. A comparative study on low-memory iterative solvers for FFT-based homogenization of periodic media. arXiv:1508.02045, 21.
URL http://arxiv.org/abs/1508.02045
Morrey, C. B., 1952. Quasi-convexity and the lower semicontinuity of multiple integrals. Pacific J. Math. 2, 2553.
Moulinec, H., Silva, F., 2014. Comparison of three accelerated FFT-based schemes for computing the mechanical response of composite materials. International Journal for Numerical Methods in Engineering 97 (13), 960–985.
Moulinec, H., Suquet, P., 1998. A numerical method for computing the overall response of nonlinear composites with complex microstructure. Computer Methods in Applied Mechanics and Engineering 157 (1-2), 69–94.
Moulinec, H., Suquet, P., 2003. Comparison of FFT-based methods for computing the response of composites with highly contrasted mechanical properties. Physica B: Condensed Matter 338 (1-4), 58–60.
Müller, W., 1996. Mathematical vs. experimental stress analysis of inhomogeneities in solids. Le Journal de Physique IV 6 (C1), C1–139.
Oppedal, A., El Kadiri, H., Tomé, C., Vogel, S. C., Horstemeyer, M., 2013. Anisotropy in hexagonal close-packed structures: improvements to crystal plasticity approaches applied to magnesium alloy. Philosophical Magazine 93 (35), 4311–4330.
URL http://www.tandfonline.com/doi/abs/10.1080/14786435.2013.827802
Ortiz, M., Repetto, E. A., 1999. Nonconvex energy minimization and dislocation structures in ductile single crystals. Journal of the Mechanics and Physics of Solids 47, 397–462.
Ortiz, M., Stainier, L., 1999. The variational formulation of viscoplastic constitutive updates. Computer Methods in Applied Mechanics and Engineering 171 (3-4), 419–444.
Park, S. H., Lee, J. H., Moon, B. G., You, B. S., 2014. Tension-compression yield asymmetry in as-cast magnesium alloy. Journal of Alloys and Compounds 617, 277–280.
URL http://dx.doi.org/10.1016/j.jallcom.2014.07.164
Pollock, T. M., 2010. Weight Loss with Magnesium Alloys. Science 328 (5981), 986–987.
URL http://www.sciencemag.org/cgi/doi/10.1126/science.1182848
Quey, R., Dawson, P., Barbe, F., 2011. Large-scale 3d random polycrystals for the finite element method: Generation, meshing and remeshing. Computer Methods in Applied Mechanics and Engineering 200 (17), 1729 – 1745.
URL http://www.sciencedirect.com/science/article/pii/S004578251100003X
Schneider, M., Ospald, F., Kabel, M., 2016. Computational homogenization of elasticity on a staggered grid. International Journal for Numerical Methods in Engineering 105 (9), 693–720, nme.5008.
URL http://dx.doi.org/10.1002/nme.5008
Shanthraj, P., Eisenlohr, P., Diehl, M., Roters, F., 2015. Numerically robust spectral methods for crystal plasticity simulations of heterogeneous materials. International Journal of Plasticity 66, 31–45.
URL http://dx.doi.org/10.1016/j.ijplas.2014.02.006
Spahn, J., Andrä, H., Kabel, M., Müller, R., 2014. A multiscale approach for modeling progressive damage of composite materials using fast fourier transforms. Computer Methods in Applied Mechanics and Engineering 268, 871–883.
Stanford, N., Sotoudeh, K., Bate, P. S., 2011. Deformation mechanisms and plastic anisotropy in magnesium alloy AZ31. Acta Materialia 59 (12), 4866–4874.
URL http://dx.doi.org/10.1016/j.actamat.2011.04.028
Tomé, C. N., Beyerlein, I. J., Wang, J., McCabe, R. J., 2011. A multi-scale statistical study of twinning in magnesium. Jom 63 (3), 19–23.
Vidyasagar, A., Tan, W. L., Kochmann, D. M., 2017. Predicting the effective response of bulk polycrystalline ferroelectric ceramics via improved spectral phase field methods. Journal of the Mechanics and Physics of Solids 106, 133–151.
Wang, J., Beyerlein, I. J., Hirth, J. P., 2012. Nucleation of elementary $\bar{1}011$ and $\bar{1}013$ twinning dislocations at a twin boundary in hexagonal close-packed crystals. Modelling and Simulation in Materials Science and Engineering 20 (2), 024001.
URL http://stacks.iop.org/0965-0393/20/i=2/a=024001?key=crossref.fb2b9a486c4b093d046f5abc11fb2e98
Willot, F., Abdallah, B., Pellegrini, Y. P., 2014. Fourier-based schemes with modified Green operator for computing the electrical response of heterogeneous media with accurate local fields. International Journal for Numerical Methods in Engineering 98 (7), 518–533.

Zachariah, Z., Tatiparti, S. S. V., Mishra, S. K., Ramakrishnan, N., Ramamurty, U., 2013. Tension-compression asymmetry in an extruded Mg alloy AM30: Temperature and strain rate effects. Materials Science and Engineering A 572, 8–18.
URL http://dx.doi.org/10.1016/j.msea.2013.02.023

Zhang, J., Joshi, S. P., 2012. Phenomenological crystal plasticity modeling and detailed micromechanical investigations of pure magnesium. Journal of the Mechanics and Physics of Solids 60 (5), 945–972.
URL http://dx.doi.org/10.1016/j.jmps.2012.01.005

Appendix A. Kinematic Compatibility in Finite Strains

Even though the problem is formulated in terms of the deformation gradient (and calculation of the deformation mapping is not required except for postprocessing), the solution is guaranteed to be compatible as follows. Compatibility requires

$$\nabla \times \boldsymbol{F} = \boldsymbol{0} \qquad \Leftrightarrow \qquad \epsilon_{KLI} F_{kL,K} = 0 \tag{A.1}$$

or, in Fourier space,

$$-ih\epsilon_{KLI}\hat{F}_{kL}K_K = 0. \tag{A.2}$$

Substitution into the equilibrium equation yields

$$\begin{aligned} -ih\epsilon_{KLI}\hat{F}_{kL}K_K &= -ih\epsilon_{KLI}\mathbb{A}^{-1}_{ik}(\boldsymbol{K})\hat{\tau}_{iJ}(\boldsymbol{K})K_J K_K K_L \\ &= -ih\frac{1}{2}(\epsilon_{KLI} + \epsilon_{LKI})\mathbb{A}^{-1}_{ik}(\boldsymbol{K})\hat{\tau}_{iJ}(\boldsymbol{K})K_J K_K K_L = 0. \end{aligned} \tag{A.3}$$

Thus, the deformation gradient field is per definition compatible.

Appendix B. Material constants for the Mg constitutive model

The material constants used for the simulations are summarized in Table B.1. The slip and twin systems in Mg are visualized in Fig B.14.

material and numerical parameters used in simulations of pure Mg							
description	parameter	value	units	description	parameter	value	units
elastic constants	κ	36.7	GPa	hardening & dissipation (pyramidal $\langle c+a \rangle$)	h_α	30	GPa
	μ	34.0	GPa		σ_∞	150	MPa
hardening & dissipation (basal)	h_α	7.1	GPa		h_{ij}	25	MPa
	σ_∞	0.7	MPa		τ_0	17.5	MPa
	h_{ij}	0.0	MPa		m	0.05	-
	τ_0	17.5	MPa		$\dot{\gamma}_0$	1.0	s^{-1}
	m	0.05	-	extension twins	h_0	1.7	MPa
	$\dot{\gamma}_0$	1.0	s^{-1}		k_{ij}	40	GPa
hardening & dissipation (prismatic)	h_α	9	GPa	simulation parameters	Δt	0.01	s
	σ_∞	85	MPa		$n_{\text{domain},\mathcal{T}}$	128^3	-
	h_{ij}	20	MPa				
	τ_0	17.5	MPa				
	m	0.05	-				
	$\dot{\gamma}_0$	1.0	s^{-1}				

Table B.1: Material parameters are adopted from Chang and Kochmann (2015) who obtained their constants by fitting to experimental results of Kelley and Hosford (1968) for individually activated slip and twin systems, together with simulation parameters.

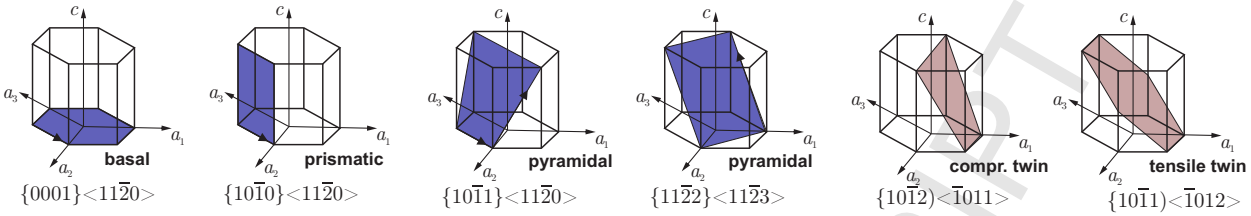

Figure B.14: Slip and twin systems in Mg.

Appendix C. Higher-order spectral corrections

As discussed in Section 3, we use modified wave vectors when taking derivatives before applying the Fourier transform with the aim to increase stability and to reduce ringing artifacts at interfaces. In order to ensure consistency, finite difference schemes are employed to derive the modified wave vectors. An example of a central difference scheme of 12th order with constant spacing Δx is

$$\begin{aligned}\frac{\mathrm{d}f}{\mathrm{d}x}(x) \approx \frac{1}{27720\Delta x}\Big[&5f(x-6\Delta x) - 72f(x-5\Delta x) + 495f(x-4\Delta x) - 2200f(x-3\Delta x)\\ &+ 7425f(x-2\Delta x) - 23760f(x-\Delta x) + 23760f(x+\Delta x) - 7425f(x+2\Delta x)\\ &+ 2200f(x+3\Delta x) - 495f(x+4\Delta x) + 72f(x+5\Delta x) - 5f(x+6\Delta x)\Big].\end{aligned} \tag{C.1}$$

Application of the discrete Fourier transform and simplification yields the approximation

$$\begin{aligned}\mathcal{F}\left\{\frac{\mathrm{d}f}{\mathrm{d}x}(x)\right\} \approx \Bigg(&-\frac{12\,i\sin(\Delta x\,h\,k)}{7\,\Delta x} + \frac{15\,i\,\sin(2\,\Delta x\,h\,k)}{28\,\Delta x} - \frac{10\,i\,\sin(3\,\Delta x\,h\,k)}{63\,\Delta x}\\ &+ \frac{i\,\sin(4\,\Delta x\,h\,k)}{28\,\Delta x} - \frac{2\,i\,\sin(5\,\Delta x\,h\,k)}{385\,\Delta x} + \frac{i\,\sin(6\,\Delta x\,h\,k)}{2772\,\Delta x}\Bigg)\mathcal{F}\{f(x)\}\\ &= \tilde{\omega}\,\mathcal{F}\{f(x)\}.\end{aligned} \tag{C.2}$$

The above approximation maintains consistency with the exact Fourier transform (where $\omega = -ihk$) in the limit of vanishing grid spacing, as can be verified through a Taylor expansion:

$$\lim_{\Delta x\to 0}\tilde{\omega} = \lim_{\Delta x\to 0}\omega\cdot\left(1 - \frac{\Delta x^{12}(hk)^{12}}{12012} + \frac{\Delta x^{14}(hk)^{14}}{27720} + O\left(\Delta x^{16}\right)\right) = \omega. \tag{C.3}$$

Extension to higher dimensions gives analogous relations, see (Vidyasagar et al., 2017). For example, if the grid spacing Δx is uniform in all directions, then $\partial f/\partial x_j$ is obtained from the above forms by replacing k by k_j, etc.

Appendix D. Derivation of the finite-difference induced regularization for a Neo-Hookean model

The introduction of finite-difference schemes for the total deformation mapping results in an approximation of the deformation gradient. For example, the following approximation holds for a second-order central difference scheme:

$$F^h_{m,N}(\boldsymbol{X}_0) = \varphi^h_{m,N}(\boldsymbol{X}_0) = \varphi_{m,N}(\boldsymbol{X}_0) + \frac{(\Delta X)^2}{6}\frac{\partial^3\varphi_m}{\partial X_N^3}(\boldsymbol{X}_0) + O(\Delta X^4). \tag{D.1}$$

We consider the elastic energy density of a Neo-Hookean solid and substitute the approximation of the total deformation gradient given by (D.1), which leads to

$$\begin{aligned}W_\mathrm{e}(\boldsymbol{F}_\mathrm{e}) &= \frac{\mu}{2}\left(\mathrm{tr}\,\overline{\boldsymbol{C}}_\mathrm{e} - 3\right) + \frac{\kappa}{2}(J-1)^2\\ &\approx \frac{\mu}{2}\left[\mathrm{tr}\left(\frac{(\boldsymbol{F}^h\boldsymbol{F}_\mathrm{in}^{-1})^T(\boldsymbol{F}^h\boldsymbol{F}_\mathrm{in}^{-1})}{(\det\boldsymbol{F}^h)^{2/3}}\right) - 3\right] + \frac{\kappa}{2}\left(\det\boldsymbol{F}^h - 1\right)^2\\ &= \frac{\mu}{2}\left[\left(\det\boldsymbol{F}^h\right)^{-2/3}\mathrm{tr}\left((\boldsymbol{F}^h\boldsymbol{F}_\mathrm{in}^{-1})^T(\boldsymbol{F}^h\boldsymbol{F}_\mathrm{in}^{-1})\right) - 3\right] + \frac{\kappa}{2}\left(\det\boldsymbol{F}^h - 1\right)^2.\end{aligned} \tag{D.2}$$

The determinant and the first invariant of the elastic deformation gradient are further expanded via a matrix Taylor series, giving

$$F^h_{m,N}(\boldsymbol{X}_0) = F_{m,N}(\boldsymbol{X}_0) + \frac{(\Delta X)^n}{(n+1)!}\frac{\partial^{n+1}\varphi_m}{\partial X_N^{n+1}}(\boldsymbol{X}_0) + O(\Delta X^{n+2}). \tag{D.3}$$

If we define

$$h^{(n)} = \frac{(\Delta X)^n}{(n+1)!}, \qquad \text{and} \qquad G^{(n)}_{iJ} = \sum_\nu \frac{\partial^{n+1}\varphi_i}{\partial X_\nu^{n+1}}(\boldsymbol{X}_0)\left(\boldsymbol{F}^{-1}_{\text{in}}(\boldsymbol{X}_0)\right)_{\nu J}, \tag{D.4}$$

then

$$\det \boldsymbol{F}^h = \det \boldsymbol{F}^h_{\text{e}} = \det \boldsymbol{F}\left(1 + h^{(n)}\,\text{tr}(\boldsymbol{F}^{-1}\boldsymbol{G}^{(n)})\right) + O(\Delta X^{n+2}) \tag{D.5}$$

and

$$\text{tr}\left((\boldsymbol{F}^h\boldsymbol{F}^{-1}_{\text{in}})^T(\boldsymbol{F}^h\boldsymbol{F}^{-1}_{\text{in}})\right) = \text{tr}\left((\boldsymbol{F}\boldsymbol{F}^{-1}_{\text{in}})^T(\boldsymbol{F}\boldsymbol{F}^{-1}_{\text{in}})\right) + 2h^{(n)}\,\text{tr}(\boldsymbol{F}^T\boldsymbol{G}^{(n)}) + O(\Delta X^{n+2}). \tag{D.6}$$

By substituting into the Neo-Hookean energy density and performing a matrix series expansion, the lowest-order error is obtained, which is reported in Section 3.3.